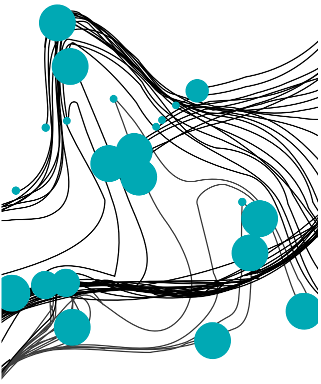

RAM ROBOTICS AND MECHATRONICS

Reduction in Controlled Degrees of Freedom for a Cable Driven Variable Stiffness Actuator

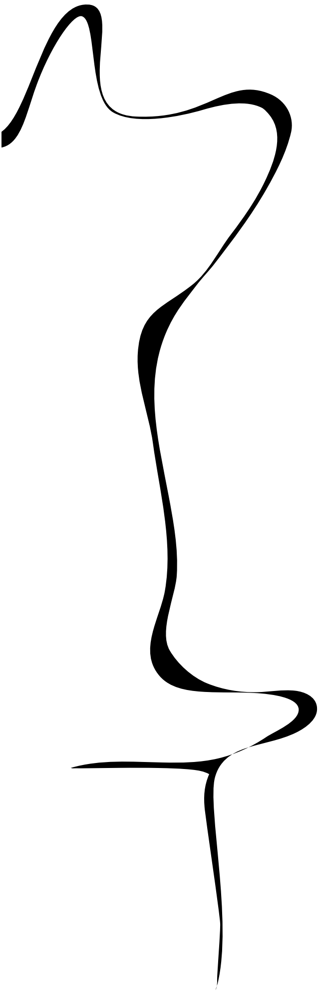

S. (Sanlap) Nandi

MSC ASSIGNMENT

Committee:
dr. ir. J.F. Broenink
dr.ir. W. Roozing
dr. ir. S.S. Groothuis
dr. ir. R.G.K.M. Aarts

April, 2020

014RaM2020
Robotics and Mechatronics
EEMCS
University of Twente
P.O. Box 217
7500 AE Enschede
The Netherlands

UNIVERSITY OF TWENTE. | TECHMED CENTRE
UNIVERSITY OF TWENTE. | DIGITAL SOCIETY INSTITUTE

Summary

Variable Stiffness Actuators (VSAs) are a class of actuators that are implemented in dynamic environments which very often involve human interaction. VSAs can change their stiffness without changing the equilibrium position which makes them suitable for the purposes of imitating physical activity of humans. Traditional stiff actuators cannot achieve such response due to their inability to interact with an unknown environment. Hence, VSAs are highly useful in these aforementioned areas where the functions of traditional actuators are inadequate.

A cable driven Variable Stiffness Actuator (VSA) proposed by Groothuis et al. (2020) contains multiple (four) degrees of freedom (DOFs). The presence of multiple actuated DOFs deems the system to be unusable as it is for its final purpose, which is to utilise it on an arm support. This system is therefore studied to evaluate the motion of the DOFs and couple them to reduce the actuated DOFs. The internal forces are investigated and are seen to be negated with coupling. The flow of energy in the system has been evaluated to do so. The total input power in the system is also assessed to check the energy-efficiency of the system.

The losses in the new system (friction) are calculated using a black-box model for analysing the efficiency of the input power. A physical prototype of the reduced DOF system is proposed whose losses are calculated. This is referred to as the theoretical model and its results are compared to the black-box model. In order to make the system energy-efficient, compensation springs were proposed, which when incorporated into the new system, would reduce these losses. The results of using compensation springs has also been analysed and it suggests that they can been used to compensate the frictional losses in the system.

This theoretical model of the new proposed system lays the groundwork for building a physical prototype and conducting experiments in the future. Recommendations are provided for practically evaluating the system's behaviour and effectively reducing its size.

Contents

List of Figures

1 Introduction

1.1 Context

The current robotics industry mostly comprises of robots that are stiff and work in a structured environment such as automation and assembly lines. Recent trends however have shown an increase in research for robotics in the fields of assistive, social and medical domain. Robots here are expected to perform tasks that would ease the burden of the human user by taking over control partially or as a whole from the user himself. In other words, they should behave in a similar manner to the humans while performing a physical task.

Human beings can effortlessly change the stiffness of muscles and joints to perform daily tasks. Traditional robots have their drawbacks due to their issues with stiffness and rigidity. They are therefore incapable of reproducing such movements as seamlessly as humans do. The characteristic that distinguishes this physical behaviour of humans to robots is known as variable stiffness. In order to replicate this behaviour in robots, variable stiffness actuators have been developed to solve the problem, wherein the robots will be able to perform the tasks which are undertaken by human beings by changing the apparent stiffness of muscles and joints.

Variable Stiffness Actuators (VSAs) are intricately designed mechatronic devices which belong to a class of compliant actuators, which means they can undergo elastic deformation. These actuators are capable of changing their apparent stiffness independent of their output position. They comprise of a number of actuated degrees of freedom (DOFs) and elastic elements in the system. The DOFs help realize the elastic elements at the actuator output. The compliant nature of the elastic elements allow energy storage which can be leveraged to achieve energy efficient actuation. The changing of the apparent stiffness can be deemed useful for various applications such as humanoid robots, manipulators and exoskeletons.

1.2 Problem Description

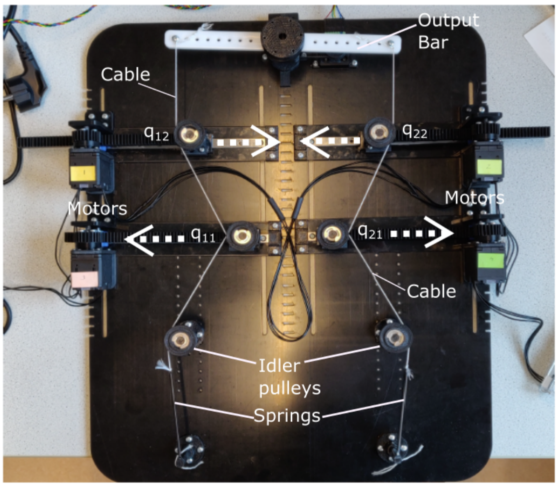

Figure 1.1: Existing VSA with four actuated DOFs (Groothuis et al. (2020))

A newly designed VSA having the capability of changing the stiffness while keeping the applied torque constant has been discussed in the paper of Groothuis et al. (2020). The current design of this VSA, as seen in Figure 1.1, is composed of four actuated degrees of freedom (DOFs). However, the system can be optimized if it were possible to reduce the number of actuated DOFs. VSAs mentioned in other literature such as Albu-Schäffer et al. (2010), Groothuis et al.

(2016), Wolf et al. (2015),Vanderborght et al. (2013) incorporate two actuated DOFs, one to control the equilibrium position and the other to control the stiffness, independently.

This VSA comprises of four linear motors which are connected to the pulleys (DOFs). When excited, the motors drive the pulleys (DOFs) horizontally over a rack and pinion. The pulleys (DOFs) are referred to as $q_{11}, q_{12}, q_{21}, q_{22}$ as indicated in Figure 1.1. There are cables routing through the pulleys, connecting them to each other, on either side of the setup which form the left and the right tendons. They are further connected to the two springs via idlers located on either tendons. The spring ends are then connected to the fixed world. The top end of the cables on either sides are connected to the output (horizontal) bar. Relocating the pulleys on the rack changes the cable tension and causes the output bar to rotate by a certain angle. This results in a change in the transmission ratio between the output bar and the springs which consequently alters the stiffness of the mechanism.

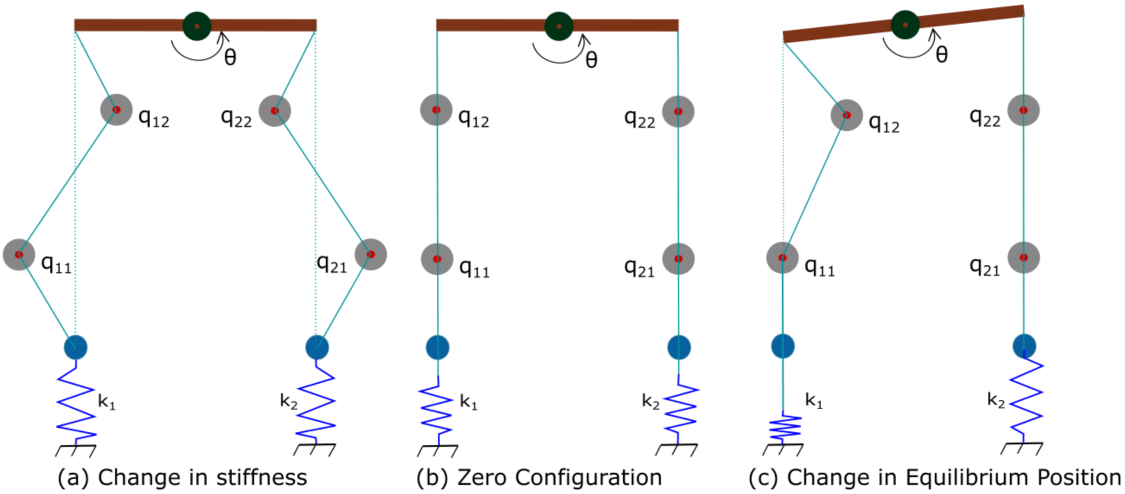

(a) Change in stiffness (b) Zero Configuration (c) Change in Equilibrium Position

Figure 1.2: Various Configurations of the VSA

The zero configuration of the system is shown in Figure 1.2b when all the components are aligned in a straight line. At this configuration the energy content of the system is zero. In the case where the top or bottom pulleys are moved simultaneously with a particular motion profile, it results in change in the stiffness (Figure 1.2a), but there in no change in the equilibrium position of the system which is indicated by the output bar. It is to be noted here that the change from zero configuration to a changed stiffness configuration requires some initial power injection. The system after reaching the changed stiffness configuration has a fixed non-zero energy content which should stay unchanged while any other stiffness change occurs over a period of time. This would deem the system to be energy efficient (Jafari et al. (2016),Visser et al. (2011)). A non-zero configuration with a particular energy content in the system caters to a specific change in the stiffness of the system. The range of the achievable stiffness for this energy level is dependent on the chosen stiffness change profile, which contributes to the motion of the DOFs and the torque around the output bar. The calculations behind this is further discussed in detail in Chapter 3.

The equilibrium position of the existing setup can be changed by relocating the DOFs unequally on either sides, left or right (Figure 1.2c). This will cause the output bar to move and a change in angle will occur. The outcome of change in equilibrium position of the output bar is identical to VSAs with lever mechanism (Groothuis et al. (2013), Jafari et al. (2011)). This signifies that on changing the point of application of the spring force, load or lever fulcrum, the apparent stiffness can be adjusted since it varies the transmission ratio between the output and the elastic element.

The elastic elements (springs) contribute to the internal forces acting in the current system. The extension and contraction of the elastic elements is a result of the movement of the pulleys (DOFs). The elastic elements (springs) store the energy that is supplied through the DOFs to the output bar. Due to the extension of these elastic elements (springs), a force is experienced by the pulleys (DOFs). These are the internal forces that are present in the system which act through the cables that are attached to the extended springs. The presence of internal forces on the DOFs means that there should be some force requirement in the opposite direction to counteract them in order to hold the pulleys (DOFs) in position. This also demands some work to be done against the forces in order to actuate the DOFs, that means there should be some injection of power at the input in order to change the stiffness. This goes against the working principle of an energy efficient system.

If the internal forces were balanced, there would be no requirement of control power to hold the pulleys (DOFs) in their position. It would then only be required to move the pulleys. Presently that is being done with the help of the linear motors that enables the pulleys to act as DOFs individually. The linear motors not only help change the equilibrium position and stiffness of the VSA, but also help compensate the internal forces which are present at each pulley (DOF) by doing work against them and holding the pulleys in position.

However having four actuated DOFs is a problem as it makes the system more complex and hence more difficult to control simultaneously during operation. From the perspective of aesthetics and compatibility, the overall system becomes bulky when four motors are used. This will become a difficulty if the system were to be integrated along with another device which may include arm supports, active prosthetics or manipulators. Therefore at present it is inconvenient to be used as it is for application purposes which involve interaction with an unknown and dynamic environment such as humans due to the large amount of DOFs present and heftiness of the overall system.

A possible solution to the problem of having excessive DOFs would be to couple them mechanically. Replacing the multiple actuated DOFs with a reduced DOF system will require some coupling mechanism. The internal forces which were being mitigated by the motors would require some other mechanism to compensate them. In practicality there will be losses due to factors such as friction which need to be reduced.

The purpose of the setup as mentioned in Groothuis et al. (2020) is primarily for its use in an arm support. The requirement for such an application is to reduce the effort on the arm for lifting or carrying a load which can demonstrate the feasibility of resembling the elbow joint motion mechanism. The motion of the elbow is controlled by the stiffness change which modulates and maintains the position (Manourat (2019)). Similarly, the VSA must be able to resemble the same operation when it is linked to the arm support. For a human being, the co-contraction of muscles on the arm help change the stiffness when holding a heavy object. This requires some effort on part of the person carrying the load on his/her arm. If a variable stiffness mechanism like the aforementioned is implemented on an arm support device, the effort generated by the person can be significantly reduced. Thus this type of device helps adjust the stiffness of the arm support to compensate the load. To follow the elbow's physiology, the change in stiffness when carrying a load should be accompanied by no change in the net torque on the elbow. Hence a choice of keeping the torque constant has been made for the design of the VSA.

1.3 Goal

The design goals are:

(1) To reduce actuated degrees of freedom (DOFs) in the system. In order to achieve this we should analyse whether the actuated DOFs in the current system can be coupled and a mechanism can be designed to accomplish this. It has to be done for a chosen stiffness profile that we want to track. The data obtained from the system's kinematic relations will be used to execute this task. This will help in solving the motion trajectories of the DOFs and analyse the power flow. Changing the chosen stiffness profile will lead to a change in the system's kinematics, which will hence provide us with a different set of results.

(2) To design an energy-efficient system. The current system loses power due to friction and due to the heating of the windings in the motors. It is essential to mitigate these losses in order to establish an energy-efficient system. For accomplishing this objective, the internal forces in the system need to be investigated initially. The losses in the system which are proportional to the internal forces can then be evaluated and a mechanism can be proposed to reduce the losses.

(3) The design should also comply to the usage objectives which are rudimentary to a VSA. They are necessities that a VSA should follow to in a specific scenario. These usage objectives are required in order to execute physically compliant behaviour in the VSA to achieve robust stiffness control and proper energy efficiency. The three usage objectives are:

1. To maintain a constant change in torque while changing the stiffness.
2. The stiffness as observed from the environment should be controlled to a desired stiffness, or, we can state that the change of stiffness should be controlled as desired.
3. The power input into the VSA through which the internal DOFs can be regulated, should be nearly equal to zero.

In order to comply to these usage objectives, the new system should follow suit of the existing system in which these objectives have already been attained. The mathematical expressions of these criteria are later discussed in section 3.1.1.

1.4 Contributions and Approach

The thesis is a continuation of the work of Groothuis et al. (2020) on *Cable Driven VIAs*. The following are the contributions to the already existing work:

1. Designing a reduced DOF system by coupling the existing DOFs. This would require modelling a new system that would have the same characteristics as the current system, while removing the four motors and replacing them with a single input. In order to build this we must study the kinematics of the existing system and apply them to the new system to check the feasibility.

   The approach mentioned above is a forward kinematic approach. By knowing the kinematics of the system, we can get an idea of the various motions and forces which govern it. This is helpful in deciding on a mechanism that can physically represent the system.

2. Identifying the losses and proposing a mechanism to compensate those losses which will help achieve the goal of having zero control power at the input, and hence establish an energy efficient system.

In order to achieve this, an estimated model of the losses and the efficiency of the new system will be computed without knowing the mechanism of the system, essentially a black-box model where we have no idea of how the system looks like. After the mechanism of the new system is defined, we can develop a clearer theoretical model of the losses and efficiency based on the mechanics. The results of this theoretical model will be compared to the estimates of the black-box model to check for its efficacy.

1.5 Outline

Following is a brief summary of the chapters in the report:

Background
Chapter 2 deals with the literature review of papers that deal with compliant actuation and variable impedance actuators (VIAs) in general. It provides a comparison between stiff and compliant actuation, the various categories of compliant actuation and variable stiffness actuators (VSAs) in particular. It also discusses the use cases of the VSAs presently in research. The concept of static balancing has been highlighted in this chapter as well which is an energy efficient force compensation technique.

System Modelling and Analysis
Chapter 3 dwells into the mathematical modelling of the VSA in question. The basic mathematical and kinematic calculations have been derived from the work of Groothuis et al. (2020), which forms the foundation of this chapter. It starts from the kinematics behind the existing system. Followed by the mathematical explanation of the usage objectives of the VSA and the flow of energy in the system. From the obatined datapoints we can then compute the motion trajectories and their corresponding equations are established and the internal forces to be compensated can be determined. These are done to inspect if coupling the system using the obtained data would result in a system whose specifications will be identical to the current system. The constancy between the input and output power has also been enumerated. An estimation has been calculated for determining the power loss in the system and the efficiency. Also it has been examined if and how compensation springs can be effective in reducing these losses.

Synthesis of DOF Reduction
Chapter 4 highlights the choice behind the design of the new system and the various components that are required to realize the system both mathematically and physically. It explains why mechanisms already present cannot be manifested to replicate the four actuated DOF model of the VSA. An overview of the new proposed system is shown. The design calculations for the components have been presented along with the explanation of how the components are going to be placed. Evaluation for the effect of friction have been done. The theoretical power loss has been compared to a black-box model in Chapter 3. The distinction between the results of the calculated losses and efficiency have been explained. The effect of the compensation springs and the efficiency of the new system has been established.

Conclusion and Future Prospects
Chapter 5 provides an insight into the conclusions that can be drawn from the research, what experiments can be performed on the new design, what results can be expected and recommendations that can help in the future developments of the system.

2 Background

2.1 Stiff vs Compliant Actuation

In certain instances of human-robot interactions, robots are required to assist humans in performing tasks or are required to perform tasks that humans can do conscientiously without any difficulty as such. Devices such as arm supports, exoskeletons, surgical robotic instruments, and humanoid robots and their subsequent actuation are all based around this concept in general which requires mimicking human attributes physically. Humans can change the apparent joint stiffness by co-contraction of agonist and antagonist muscles, the robots that are supporting such behaviour must also possess the same characteristics. This is to ensure that the robots that are assisting humans in performing the tasks can imitate the movements and perform these actions in conjunction to the users.

In traditional industries the robots that are used have a fixed compliance and are therefore stiff. The high rigidity enables precision in positioning or tracking of predefined trajectories, but does not allow enough mitigation of shock absorption or explosive movements which is essential constituent of physical human behaviour. Also once the actuator reaches a certain position, it remains stationary there, irrespective of the force (within the limits of the device) applied on it. If excessive force is applied, it can lead to dysfunctional behaviour and may cause damage the robot or even worse harm the user - the human, causing serious injuries (Liu et al. (2019), Ham et al. (2009)).

Keeping in mind all these limitations of such stiff actuators, a different class of actuators were proposed in order to mimic physical human behaviour. These are known as compliant actuators or variable impedance actuators (VIAs) (Ham et al. (2009)), which solved the problems that arise as a result of the rigidity, and the safety issues that are related to the traditional actuators. Inherent compliance actuators that constitute a subgroup of VIAs comprise of passive or intrinsic compliant element connected in series with an actuator. This can be further classified as fixed compliance for eg. Series Elastic Actuators (SEAs)(Pratt and Williamson (1995)), which cannot change its stiffness and adaptable compliance for eg. Variable Stiffness Actuators (VSAs), where stiffness can be changed by re-configuring the system mechanically (Spagnuolo et al. (2017),Vanderborght et al. (2013)).

VIAs are actuators that can change their equilibrium position and rely on forces acting externally and mechanical characteristics of the actuators such as stiffness, damping and inertia. All these three factors contribute to the impedance and hence the name. They have a high range of bandwidth and accuracy as opposed to stiff actuators. Amongst them are VSAs and SEAs that are different in nature to each other. SEAs have a compliant element attached in series to a rigid material and doesn't change its stiffness. On the other hand VSAs have the capability of changing the stiffness of their elastic element (Spagnuolo et al. (2017)).

The benefit of VSAs (not all VIAs in general) is that equilibrium position and apparent stiffness can be changed independently. By controlling the energy flow from the motors, the stiffness can be regulated and improve force accuracy while interacting with the operator which can help in keeping collisions and effect of external forces in check (Jafari (2014)).

However in Groothuis et al. (2020), SEAs are not categorized under VIAs. Rather the classification states that compliant actuators fall under two categories, fixed i.e SEAs and variable i.e. VIAs. VSAs and Variable Damping Systems fall under the subcategory of VIAs.

Besides passive mechanical compliance as described above, compliant behaviour may also be achieved through control. The compliant performance of such a system is limited by high frequency or high speed operations.

Passive compliance has the advantages of energy efficiency, quick response and simplistic control. It is subdivided further into three modes, referred to in Liu et al. (2019):

1. Varying the effective length of the elastic material
2. Lever mechanism Principle
3. Antagonistic Principle

2.2 Active and Passive Compliance

This section emphasizes on the general characteristics of the VSAs at present that describe their mechanical behaviour such as stiffness, impedance, admittance, compliance and damping. It describes how this makes them different from the rigid actuators already present for robotic applications. These attributes enable the VSAs to replicate the physical movements of a human or animal, thus making it more suitable for such purposes as mentioned in Vanderborght et al. (2013).

2.2.1 Active Impedance

Active impedance involves the imitation of an impedance behaviour with the help of a controller which is a software (Loughlin et al. (2007)). The output state is measured and the error is corrected by the controller that can then be utilized by the actuator. The drawback though of this kind of an approach is its energy efficiency as it cannot store energy. Since energy cannot be stored, this technique cannot be implemented for energy efficient actuation such as passive robots or actuators which will require the help of external energy. Also the bandwidth is quite limited which will make it problematic for shock absorption. Limited bandwidth may cause the mechanisms such as gearboxes and bearings to break under the influence of high peak torques or cause fatigue on the entire structure. The control is often complicated and requires meticulous models for system dynamics. The benefit of active impedance however is its ability to adapt to the varying damping and stiffness (impedance) of the system on a theoretical level, which means it can be adjusted online depending on the situation. The mechanical system associated with such an approach is also not complex because there are no extra elastic elements required, nor any additional DOFs to achieve this.

2.2.2 Fixed Compliance

The fixed compliant actuators that are being dealt in this section are ones having elastic elements connected to actuators or drive trains in series. The most common example of an actuator with fixed compliance is the Series Elastic Actuator (SEA) (Liu et al. (2019)). It comprises of a spring attached to a stiff actuator in series. The choice of the spring determines the stiffness of the actuator and hence the physical stiffness cannot be adjusted during operation. Such mechanisms usually comprise of a more complex system design that involve energy storage and shock absorption as resulting system properties with the addition of elastic elements. They usually have low intrinsic damping and makes the use of an extra damping component or the damping is effectuated with the help of control (Petit and Albu-Schäffer (2011)).

2.2.3 Adjustable Compliance

Adjustable compliance refers to the control of stiffness by the reconfiguration of mechanical components present in the system. This also involves of the use of elastic elements for storing and releasing energy. Variable stiffness actuators (VSAs) are an example of actuators that implement adjustable compliance for achieving their desired behaviour. Unlike stiff actuators it has the liberty to change its equilibrium position due to the influence of forces acting externally and the mechanical characteristics of the actuator such as stiffness or damping. Such an approach additionally increases the bandwidth that enables better shock absorption. In such cases two motors that are required, one to control the equilibrium position while the other to

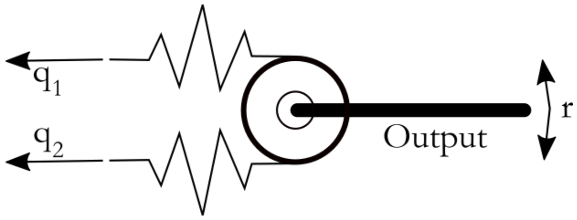

Figure 2.1: Antagonistic setup of a VSA (Groothuis et al. (2020))

control. This can be further classified into the following categories as defined in Vanderborght et al. (2013):

Spring pre-load: The pre-load or pretension on the spring is adjusted in order to change the stiffness. This comprises of the following subcategories :

- **Antagonistic springs with antagonistic motors:** Refer to Figure 2.1. Requires two non-linear springs, where the springs and the motors are placed in an antagonistic setup. The motors move in the opposite direction to change the equilibrium position and in the same direction to change the stiffness.
- **Antagonistic springs with independent motors:** Almost same as the previous type but the motors decouple the control of stiffness and equilibrium position partly. It comprises of two motors which have to work in a synchronous manner to change either the stiffness or the equilibrium position. This means that if one of the parameters is being adjusted the other can't be done so simultaneously.
- **Pre-load adjustment of single spring:** Comprises of two motors. It does not belong to the antagonistic class. The stiffness is controlled by a motor attached to one linear spring whose pre-load is altered while the other motor changes the equilibrium position.

The VSA at present is an antagonistic setup (Laffranchi et al. (2009),Petit et al. (2010)) that comprises of linear springs and two motors on either side (four in total). The system is symmetric so that means there are two motors on the left and two on the right tendons as seen in Figure 1.1. Considering the left side, one of the motors control the stiffness and the other one to changes the equilibrium position for the left side. While the other two motors on the right side work in the exact identical fashion. When all the four motors are actuated at the simultaneously, all the four DOFs act together to change the position and stiffness.

Changing Transmission between load and spring: This comprises of systems that change the transmission ratio between the output and the internal spring which adjusts the stiffness. In such a system there is no pretension on the spring. The force on the spring is perpendicular to its displacement and hence no external energy is required for changing the stiffness (dot product of two perpendicular vectors is zero) in the ideal case. In real world applications however, some external energy is required to overcome friction which can be reduced by techniques such as material choice. The transmission ratio can be changed in three ways namely, changing the pivot point on the output, changing the point of application of force on the output or changing the position of the spring on the output. Lever-arm based VSAs (refer to figure 2.2) use this type of an approach.

Physical Properties of the spring: The stiffness of a spring (K) is given by $K = \frac{EA}{L}$, where E is the Young's modulus, A is the cross-section area and L is the effective length of the spring. Either of them can be changed to alter the physical characteristics of the spring. But changing the physical properties of the spring other than its length or area would require choosing materials whose Young's Modulus (E) can be altered effectively by the application of external paramet-

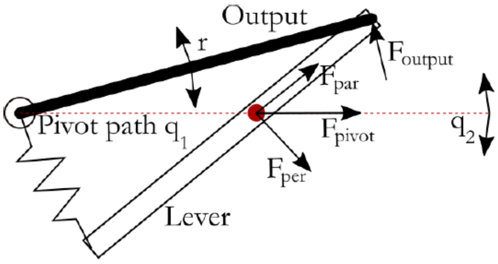

Figure 2.2: Lever-arm Based VSA (Groothuis et al. (2020))

ers such as change in temperature or pressure. But such measures are extremely difficult and therefore there are no examples of VSAs implementing such approach.

2.3 Present VSAs and their Usage

2.3.1 Use Cases

The work done in the paper, Wolf et al. (2015), deals with VSAs in general, use cases are the applications for which VSAs are intended to be used. These are considered as the stepping stones for the designing of the VSAs including choice of parameters and components. These most common use cases are as follows:

- **Shock absorption :** It is the ability of a material to resist impacts without sustaining damage. In robots there maybe high peak torques on the actuator output as a result of the large inertial forces and fast operations. Even with very stiff robots the impact of the collisions cannot be mitigated. VIAs are used as buffers to absorb the shock or impact that the robots face. They are connected in between the output link of the robots and the gearbox. This is different in traditional robots where the link would be directly connected to the gearbox. The VIAs comprise of an elastic unit that acts as a shock absorber. They can be a spring, a damper or a combination of both. VSAs are basically VIAs with only a spring component and no damping component.

- **Stiffness variation at constant load :** For effective force/torque interactions with the external world, the stiffness variation at constant load is required. The surface structure determines what stiffness setup would suit it the best and minimize the error. A surface with large stick-slip friction will be well suited for higher stiffness setups, whereas an uneven surface can make the use of less stiffness.

- **Stiffness variation at constant position :** Similar to muscular co-contraction, changing stiffness at constant load is done to obtain a low position error which may occur as a result of disturbance. Take the example of a hand holding a glass of water in free space and an external object hits the hand, the muscles will co-contract and stiffen in order to not let go of the glass or spill the water. So this kind of technique is primarily used to optimize the disturbances.

- **Cyclic movements:** These involve the repetitive acceleration and deceleration of the robots. The advantage of such movements are that the positioning motors that drive the actuators have to execute smaller movements as compared to the desired output trajectory which would make the system energy efficient. For cases where a trajectory that is perfectly matching only friction and damping losses of the VSA have to be compensated by the motors. Walking and jumping are some examples of cyclic movements. But furthermore such movements can be adapted accordingly and changed in robots by tuning the motor parameters with the help of controls.

- **Explosive movements:** The characteristic of explosive movements in robots is a result in high acceleration at the output due to a large increase in the velocity over a relatively short period of time. VSAs have the ability to drive the motors at a velocity above their peak velocity thus accelerating the actuator output. By blocking the actuator output and using the motors to apply a torque it is possible to store potential energy in the springs by pre-loading them. This energy can then be released by unblocking the output in the form of kinetic energy. It is important for the VSA to have a good energy storing capability. It is useful to therefore start with a low stiffness and then gradually increasing it during the operation phase. The maximum output velocity is defined as the sum of the maximum velocity of of the joint positioning motors and the velocity gained by unloading the maximum potential energy of the spring (Wolf et al. (2015)). Changing the gear ratio of the positioning motor can change the output velocity but will effect the maximum output torque. If the motor torque is high and stiffness is large, then the bandwidth of the VSA will be large.

2.4 Static Balancing

Since the system which has been proposed is approximated to be quasi-static in nature, the work of Herder on static balancing is of significance. In these systems force and energy balancing becomes the highlight as the system has to be actuated by conserving energy. These can be observed from the works in the papers Herder et al. (2011), Barents et al. (2011), Herder (2001).

Concepts regarding the principles have been discussed in the paper Herder et al. (2011). The example of a basic gravity balancer is a simple way of demonstrating a physical model where the static balancing condition can be met.

$$mgL = kar \tag{2.1}$$

where m = mass of the balancer payload, g = acceleration due to gravity, L = length of the balancer, a = Vertical length from fixed end of balancer to fixed end of spring, r = Distance between fixed end of balancer and point where the spring is attached to the balancer.

Figure 2.3 shows a gravity balancer and its various components. It is a fundamental example of a statically balanced system. From equation 2.1 the balance condition of the system with respect to the gravity can be observed. The left side of the equation represents the force acting on the system (which is basically a horizontal bar) due to gravity multiplied by the length of the bar. This provides a torque component of the bar. To balance this out on the right hand side of the equation the variables k, a and r are present which also provides another torque component that helps in balancing the system. When the torques are equal or in other words the net torque is zero, the system is statically balanced. On changing the values of a and r the balance conditions of the system can be altered accordingly. Also values of k,L and different masses m can affect the conditions, but more often the change of the length of the balance spring s which is dependent on a,r and the output angle ϕ which is the angle between a and r as shown in Figure 2 and given by the equation:

$$s = \sqrt{a^2 + r^2 - 2ar\cos\phi} \tag{2.2}$$

Statically balanced systems can actuate in the presence of considerable amount of forces, but don't require any operating force or energy because the resulting net force is (close to) zero. The exchange of energy between the storage elements present in the system are considered perfect and hence the only energy that is required for operation is external to compensate losses such as friction, and also accelerate or decelerate the process. Henceforth they are designed to maintain constant potential energy throughout their range of motion making use of springs and counterweights.

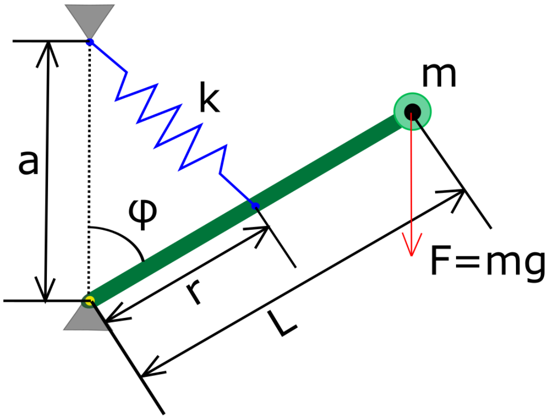

Figure 2.3: Static Balancing of a Gravity Balancer

2.4.1 Application of Static Balancing to VSA Mechanisms

The present setup of the VSA comprises of springs which contributes to forces acting on the DOFs along the cables that connect them. The profiles of these forces were found to be non-linear as will be discussed in detail later in the report. There will be losses due to friction that will be proportional to these forces. Due to the losses on the DOFs, work has to be done to actuate the DOFs, which involves generating force from an external input like a hand crank or motor. Using static balancing techniques to the DOFs may be a remedy to this. If designed properly this will enable the compensation of losses which would mean the energy required to actuate the system is close to or equal to zero.

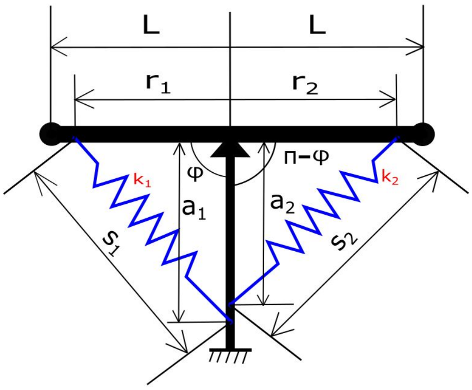

Figure 2.4: Spring to spring balancer

The most probable design for force balancing in the current system would be the use of spring to spring balancers as mentioned in Barents et al. (2011). This comprises of a gravity balancer with springs on each side compensating each other. Since there is no effect of gravity on the VSA due to its planar orientation, such an implementation of spring balancers may prove useful in counteracting the losses that are acting on the system. This is illustrated in Figure 2.4 and the balance condition can be computed as follows:

$$k_1 a_1 r_1 = k_2 a_2 r_2 \tag{2.3}$$

where k_1 = Stiffness of first spring, k_2 = Stiffness of second spring, a_1 = Vertical length from fixed end of balancer to fixed end of first spring, a_2 = Vertical length from fixed end of balancer to fixed end of second spring, r_1 = Distance between fixed end of balancer and point where the first spring is attached to the balancer, r_2 = Distance between fixed end of balancer and point where the second spring is attached to the balancer.

Since the system at hand is symmetric the net torques are likely to cancel out each other when springs are attached. So the system will always be in equilibrium at its starting position.

2.5 Conclusion

The literature study related to the work done in the fields of compliant actuation and mechanisms related to force balancing which are closely related to the topic at hand, have been presented in this chapter. Based on the aforementioned, a clear idea can be gained on how to proceed with the system. The knowledge can be implemented to acquire a system which would have reduced actuated DOFs where the internal forces are statically balanced. Energy efficient actuation has been a field of study in a few of these papers, where the apparent stiffness change will not change or influence the overall potential energy that is stored in the elastic elements of the system. But to achieve this energy efficiency along with the former challenges of reducing the actuated DOFs and compensating reaction forces from the cables is something that has not been attempted by any of these researches and is henceforth a matter to be investigated.

3 System Modelling and Analysis

In this chapter we will deal with the existing system and its kinematics. The kinematic equations and mathematical conditions up until the end of Section 3.1.1 will implement the work of Groothuis et al. (2020). The data obtained from his work will be useful to determine the motion trajectories of the individual DOFs, which is essential for obtaining the stiffness change profile identical to the existing system, for a new system with reduced DOFs. Furthermore, we will compute the internal forces in the system to inspect the losses in the reduced DOF system. This essentially will help in deciding whether there is a use for any compensation techniques in order to negate these forces. For this reason, the power loss of the system will be modelled. An estimate of the efficiency of the power input will be calculated to establish an idea for the new system.

3.1 Kinematics of the Existing system

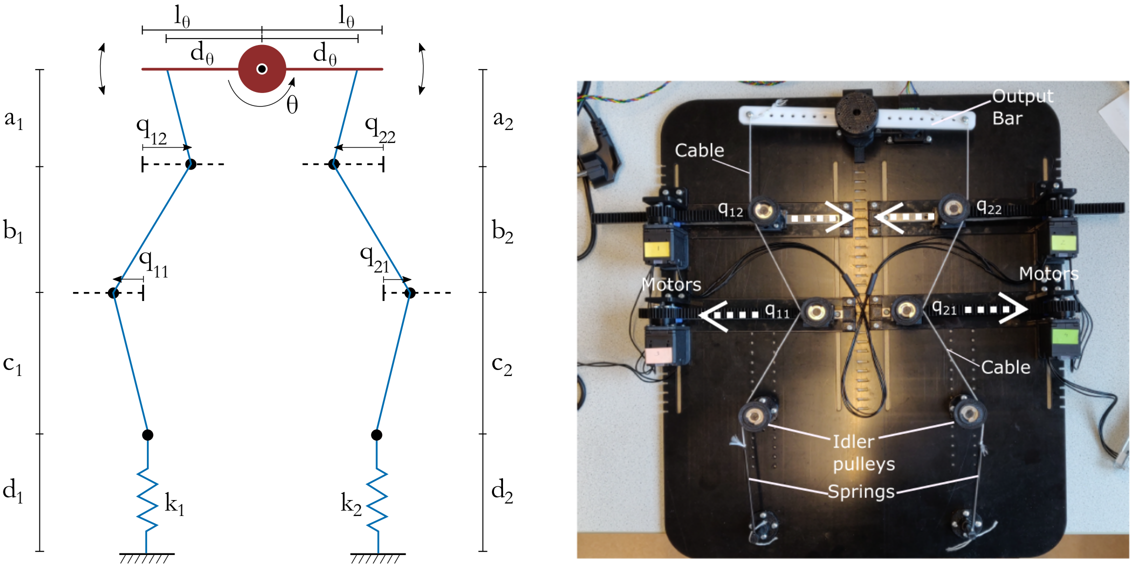

(a) Schematic Diagram of Existing VSA

(b) Existing VSA in real life

Figure 3.1: Schematic Diagram vs Real Life Model Comparison of the Existing VSA.

Figure 3.1 shows the comparison schematic model and the physical model of the existing VSA. In figure 3.1a, the two springs attached to the end of the cables are denoted as k_1 and k_2. The cable routing all the components is assumed to be infinitely stiff (zero compliance) such that it has ideally zero effect on the system's performance due to its negligible elasticity.

As discussed in the Chapter 1, there are four movable pulleys in the entire system which are the internal degrees of freedom, referred to as $\boldsymbol{q}$. They are positioned such that the system is in the equilibrium condition and can be moved horizontally along the dashed lines which are indicated in the Figures 3.1a and 3.1b. When the actuated DOFs along with the springs are aligned in a straight line with respect to each other, it is denoted as the zero configuration of the system that is $q_{11} = q_{12} = q_{21} = q_{22} = 0$ (Figure 1.2 (b)). At this configuration the length of the tendons are the shortest since the spring extension is minimal. The system is constructed such that $d_\theta = l_\theta$, where d_θ is the length between the endpoints of the cables connected on the output bar and l_θ is the length of the output bar (refer to Figure 3.1a).

Changing the positions of the internal DOFs causes a deflection of the output bar, that results in a change in the output angle θ (indicated in Figure 3.1a) and also the output stiffness K_θ

(refer to Groothuis et al. (2020)). The desired output- stiffness change profile is a choice the user makes and can be chosen so as to the keep the desired stiffness change within a certain range. For the above model, $\dot{K}_{\theta_{des}} = A_m \cos(t)$, where A_m is the amplitude of the stiffness in Nm/rad/s and t is the time period in seconds, was chosen for an initial configuration (which is a non-zero configuration as seen in Figure 1.2 (a)) where the system would be at an equilibrium position for time $t = 0$.

The motion trajectories of the DOFs due to the choice of the stiffness profile are also dependent on the length of the tendons. The change in length of the tendons is a consequence of the change in length of the springs attached to the ends of the cables.

The value of the extended spring length, s_i, is determined by:

$$s_i = L_i(\boldsymbol{q},\theta) - \overline{L_i} \tag{3.1}$$

Where $\overline{L_i}$ is the equilibrium configuration in which the spring is in a zero-deflection state and the angle of the output bar θ is 0. This implies that at the zero configuration state there is no energy stored in the spring. This is true when $s_i = 0$, which means at this instance $L_i(q,\theta) = \overline{L_i}$. Energy of a spring is mathematically expressed as $H(s_i) = \frac{1}{2}k_i s_i^2$. So if $s_i = 0$ then $H(s_i) = 0$.

From Figure 3.1a the value of the length of the tendons on the left and right side denoted by L_1 and L_2 respectively are calculated by:

$$L_1(\boldsymbol{q},\theta) = d_1 + \sqrt{c_1^2 + q_{11}^2} + \sqrt{b_1^2 + (q_{11} + q_{12})^2} + \sqrt{(-l_\theta + d_\theta \cos\theta + q_{12})^2 + (a_1 - l_\theta \sin\theta)^2} \tag{3.2}$$

$$L_2(\boldsymbol{q},\theta) = d_2 + \sqrt{c_2^2 + q_{21}^2} + \sqrt{b_1^2 + (q_{21} + q_{22})^2} + \sqrt{(-l_\theta + d_\theta \cos\theta + q_{22})^2 + (a_2 + l_\theta \sin\theta)^2} \tag{3.3}$$

where, L_1, L_2 = Total length of the tendons on the left and right sides respectively.
a_1,b_1,c_1,d_1 and a_2,b_2,c_2,d_2 = individual length of the cables and springs that constitute the tendons of the left and right sides respectively as seen in Figure 3.1a.

The output stiffness and torque can be derived from the total energy stored in the system. Considering elastic elements to be linear, the Hamiltonian Energy can be defined as a function of the elastic elements (extended spring lengths s_1 and s_2), which is the sum of the left and right stored potential energies.

$$H(s_1, s_2) := \frac{1}{2}k_1 s_1^2 + \frac{1}{2}k_2 s_2^2 \tag{3.4}$$

$$H(s_1, s_2) = \frac{1}{2}k_1 (L_1(\boldsymbol{q},\theta) - \overline{L_1})^2 + \frac{1}{2}k_2 (L_2(\boldsymbol{q},\theta) - \overline{L_2})^2 \tag{3.5}$$

The output torque can then be written as:

$$\tau_\theta(\boldsymbol{q},\theta) = \frac{\partial H(s_1, s_2)}{\partial \theta} = k_1(L_1(\boldsymbol{q},\theta) - \overline{L_1})\frac{\partial L_1(\boldsymbol{q},\theta)}{\partial \theta} + k_2(L_2(\boldsymbol{q},\theta) - \overline{L_2})\frac{\partial L_2(\boldsymbol{q},\theta)}{\partial \theta} \tag{3.6}$$

The change in the output stiffness is dependent on the change in the output torque (τ_θ) of the output bar with respect to the change in the angle θ. The output stiffness linearized around a configuration $\overline{\theta}$ and modelled as a function of the pulley positions $\boldsymbol{q}$ has been mathematically represented as:

$$K_\theta(\boldsymbol{q},\overline{\theta}) = \frac{\partial \tau_\theta(\boldsymbol{q},\theta)}{\partial \theta}\bigg|_{\theta=\overline{\theta}} \tag{3.7}$$

3.1.1 Satisfying Usage Objectives

This subsection comprises of the mathematical expressions of the usage objectives of a VSA explained previously in section 1.3. Therefore the new system that is to be designed must fit the requirements of :

- Having a controlled change in the stiffness from the environment such that it equals the desired change in stiffness.
- Keeping the torque constant.
- Keeping the change in energy constant.

The above requirements can be formulated as:

$$\dot{K}(t) = \dot{K}_{des}(t) \tag{3.8}$$

Where $\dot{K}(t)$ is the stiffness change obtained from the environment at the output of the system and $\dot{K}_{des}(t)$ is the desired change in stiffness, both at a time t.

Due the change in stiffness the output torque, (or force) changes if it is non-zero. The change should be regulated as desired:

$$\dot{\tau}(t) = \dot{\tau}_{des}(t) \tag{3.9}$$

Where $\dot{\tau}(t)$ is the initial change in the output torque as defined by the model in equation 3.6 and $\dot{\tau}_{des}(t)$ is the desired change in torque, both at a time t.

The injection of energy or power (P_{control}) into the VSA through the control port must be ideally equal to zero. The control port is the input of the system through which energy is provided to help actuate the DOFs. It helps control the configuration of the internal DOFs of the system. Mathematically over a time period t, this can be represented as:

$$\int_0^t P_{\text{control}}(\zeta)\, d\zeta = 0 \tag{3.10}$$

The flow of energy has been described more elaborately in section 3.4.

In the work of Groothuis et al. (2020) it was considered that the output stiffness could be changed without changing the output force or torque i.e.:

$$\dot{\tau}(t) = 0 \tag{3.11}$$

This was simply a choice and was also followed for the new proposed design of the VSA.

3.2 Degree of Freedom Motions

The usage objectives, as discussed in section 3.1.1 were already proven in Groothuis et al. (2020). It is mentioned from his work that a system with n number of elastic elements when plugged into the equations 3.8, 3.10, 3.9 resulted in a set of first degree, first order, non linear differential equations. This comprised of a set of data points or values that were interpolated over a certain time window and plotted.

Since the differential equations were non-linear in nature, of the form $f(\boldsymbol{q})\dot{\boldsymbol{q}} = 0$, it could not be solved for $\boldsymbol{q}$ analytically. Hence, they had to be solved numerically. The plots were obtained from the work of Groothuis et al. (2020), where a certain stiffness profile change was chosen in order to numerically solve the individual equations for each of the internal DOFs.

The equations of motion have to be periodic in nature since the initial desired stiffness $\dot{K}_{\theta_{des}}$=$0.5\cos(t)$ was chosen as such [1]. The simulated motion trajectory that was already available from the obtained data points are seen in Figure 3.2. The present system motion already

---

[1] In the paper of Groothuis et al. (2020), $\dot{K}_{\theta_{des}} = 0.3\cos(t)$. With the corresponding dimensions of the existing system, it was difficult to realize a new physical model with reduced DOF. The values of the dimensions were therefore increased and a larger amplitude A_m could be chosen to fit the components.

met the conditions for the stiffness profile change, output torque and power injection at the control port (Figure 3.3). The range of the stiffness is dependent on the energy content (discussed later in 3.4) of the system. The stiffness change can be seen in the plot to have maximum and minimum value since it follows a periodic trajectory. The range of the stiffness is dependent on many factors which includes choice of the stiffness change profile, the length of the tendons and also the choice of the stiffness of the elastic elements attached at the end. All these factors cumulatively contribute to the limits of the achievable stiffness for that energy level. The data points used for plotting these motion trajectories were available and therefore could be used to find an approximate function or equation that governs the motion of the system mathematically. The differential equations describing the mathematical model of the system were solved numerically.

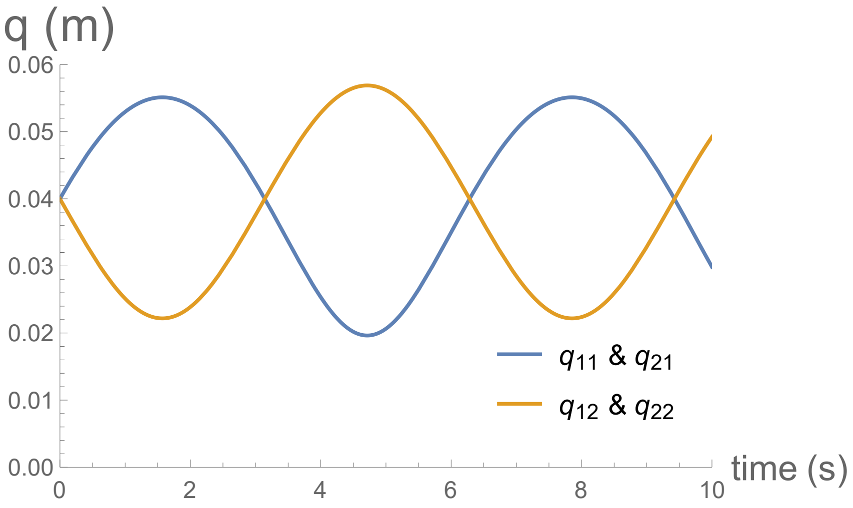

Figure 3.2: The q trajectories that solve the three objectives simultaneously for a desired stiffness change profile of $\dot{K}_{\theta_{des}} = 0.5\cos(t)$.

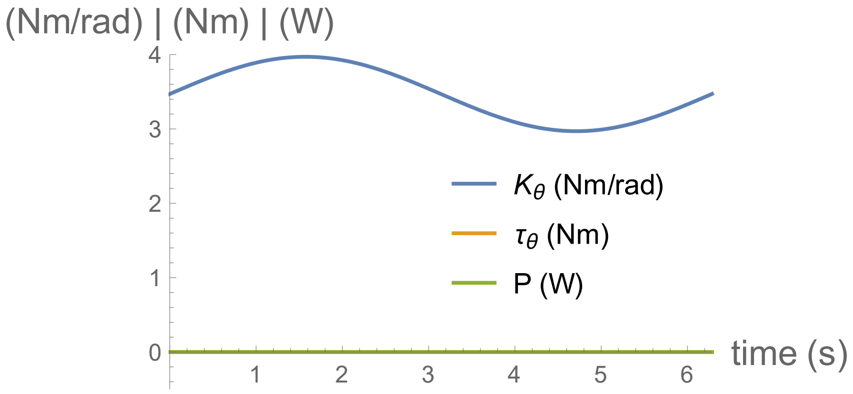

Figure 3.3: Stiffness profile, output torque and power injection with respect to time for $\dot{K}_{\theta_{des}} = 0.5\cos(t)$.

A curve fitting was applied to a set of data points using MATLAB that were already available from the data points plotted in Figure 3.2. In this case a Fourier series was chosen to approximate the data points on the curve to obtain an analytical equation. Due to the fact that the desired stiffness change profile was a cosine function, it would make sense that the resulting trajectories of the DOFs that define this change would be periodic in nature. A Fourier series is a periodic function comprising of a summation of sinusoids that would suit the given conditions. Hence, the curve fitting using a Fourier series was the best way to derive an approximate analytical equation that would satisfy the motion of the system, which can later help in further studying the system and analysing the results of its behaviour. This resulted in an approximated Fourier series function for the motion of the pulleys with the following expression:

$$q = a_0 + a_2\cos(t) + a_4\cos(4t) + b_1\sin(t) + b_3\sin(3t) + b_5\sin(5t) \tag{3.12}$$

where, q = position of the pulley (DOF); $a_0, a_2, a_4, b_1, b_3, b_5$ = Co-efficients of the function for the analytical equation.

The Fourier series comprised of values upto the fifth harmonics of the base frequency, and the values have been truncated to 6 terms since the higher frequency components are negligibly small [2]. The q values define the position of the the DOFs (pulleys) traversed, in meters.

In reference to plots in Figure 3.2, it can be observed that the trajectories of bottom DOFs, q_{11} and q_{21} are the same whereas, the DOFs at the top, q_{12} and q_{22} are alike (but slightly different from the top two pulleys) and 180° out of phase when compared to the other two. This behaviour in motion occurs due to the fact they are aligned symmetrically at a starting position of $q_{11} = q_{12} = q_{21} = q_{22} = 0.04$ m at time $t = 0$. The starting position can be verified in Figure 3.2. The phase shift is due to the reason that the top two DOFs traverse inwards as compared to the bottom two which move outwards.

By using curve fitting the approximate analytical equations of these trajectories for a time t were found to be:

$$\begin{aligned} q_{11}(t) = q_{21}(t) =& 0.0387178 + 0.00131169\cdot\cos(2t) - 0.0000305498\cdot\cos(4t) + \\ & 0.0175825\cdot\sin(t) - 0.00015739\cdot\sin(3t) + 5.28572\cdot10^{-6}\cdot\sin(5t) \quad (3.13) \\ q_{12}(t) = q_{22}(t) =& 0.0397704 + 0.00023253\cdot\cos(2t) - 3.0255\cdot10^{-6}\cdot\cos(4t) - \\ & 0.0172983\cdot\sin(t) + 0.0000551443\cdot\sin(3t) - 4.64409\cdot10^{-7}\cdot\sin(5t) \quad (3.14) \end{aligned}$$

The output stiffness, output torque and input power can be calculated when these trajectories are used as motion profiles for the DOFs. The motion profiles of the top two pulleys and similarly the bottom two pulleys are identical in nature. The resulting functions are non-monotonic many-to-one (cyclic). They are synchronous to each other, where the motion of top two DOFs are 180° out of phase with the bottom ones, but has the same frequency. There is no phase difference between q_{12} and q_{22} and likewise between q_{11} and q_{21}. These conditions of synchronicity make it possible to couple the DOFs by mechanical means in order to actuate simultaneously as a function of time by the help of reduced (one or two) actuated DOFs. The difference in the motion profiles between the top and the bottom pulleys is by design.

3.3 Internal Forces and Compensation

The force on the system generated by the springs, k_1 and k_2, that are attached to the end of the bottom pulleys as seen in Figure 3.1a due to the elongation is caused by the re-positioning of the pulleys (DOFs) during the operation of the system. The spring force is given by Hooke's Law:

$$F_i = k_i s_i \tag{3.15}$$

where, F_i = Spring force, k_i = Stiffness constant (100 N/m), s_i = Extended length of spring, and $i \in \{1,2\}$

Due to the force generated by the springs, the cables attached to the DOFs(pulleys) exert a force on them. The force acting on the pulleys can be divided into the horizontal and vertical components. The vertical component is however compensated by a counteracting force that constrains the pulleys from moving out of their horizontal DOFs. The horizontal forces can be calculated for either side and they are equal in magnitude due to the symmetric design of the

---

[2] The neglected values comprised of those having a value of $<10^{-7}$. The relative error due to this was 0.12%.

system. Therefore considering the left side, the force acting on each of the pulleys is calculated as (refer to Figure 3.4) :

$$F_{net_{q_{12}}} = F_i(\cos\alpha + \cos\beta) \tag{3.16}$$

$$F_{net_{q_{11}}} = F_i(\cos\beta + \cos\gamma) \tag{3.17}$$

where, α and β are the angles of the cable/tendon with respect to the horizontal, for the segment originating from the pulley corresponding to the DOF q_{12}. Similarly γ is the angle corresponding to the DOF q_{11} respectively. Owing to the geometry of the system the angle β is a corresponding angle (hence equal) and is observed at two places. It is formed by the cable/tendon with respect to the horizontal and corresponds to q_{12} at the top and q_{11} at the bottom. $F_{net_{q_{12}}}$ is the net force acting on q_{12} and $F_{net_{q_{11}}}$ is the net force acting on q_{11}.

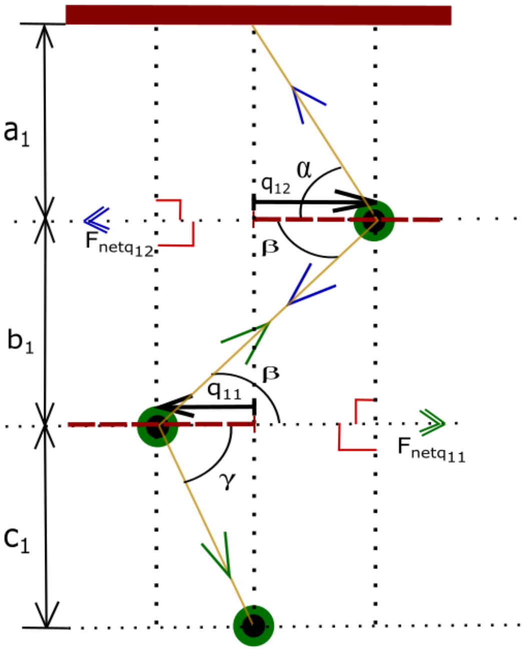

Figure 3.4: Schematic cut section diagram of the decomposition of forces acting on the pulleys on the left side of the system as seen in Figure 3.1a.

The values of the various angles that are projected by the pulleys can be calculated depending on the values of the constant perpendicular lengths of the the cables as denoted by a_i,b_i,c_i where $i \in \{1,2\}$ to indicate right or left side and the value of the position of the DOF (pulley) q_{ij} (where $i, j \in \{1,2\}$) which indicates which pulleys are taken into consideration.

Therefore, we can find the angles for the left side of the system as follows:

$$\alpha = \arctan\left(\frac{a_i}{q_{12}}\right) \tag{3.18}$$

$$\beta = \arctan\left(\frac{b_i}{q_{12} + q_{11}}\right) \tag{3.19}$$

$$\gamma = \arctan\left(\frac{c_i}{q_{11}}\right) \tag{3.20}$$

Similarly, for the right side the angles can be calculated in the identical manner.

Since the system is symmetric, the forces on the left side are equal to ones on the right and can therefore be expressed as:

$$F_{net_{q_{12}}} = F_{net_{q_{22}}} \tag{3.21}$$

$$F_{net_{q_{11}}} = F_{net_{q_{21}}} \tag{3.22}$$

Plotting the net forces with respect to time as seen in Figure 3.5 it can be observed that the forces acting at the top pulleys are identical to each other as expected. Same goes for the two bottom pulleys. In the existing system, these forces are compensated with the help of motors. If these motors were to be removed in order to reduce the DOFs, there would be need for a mechanism to compensate these forces provided the system is imperfectly coupled, which means the internal forces are not statically balanced or cancelled out by the coupling mechanism that is being implemented. A coupling mechanism will implement a mechanical device that will essentially connect the four DOFs together such that they can be actuated simultaneously. Nonetheless, if a perfect coupling of DOFs can be achieved keeping the angle $\theta = 0$, thus keeping the change in energy content of the system zero, these forces would be counteracted as a result.

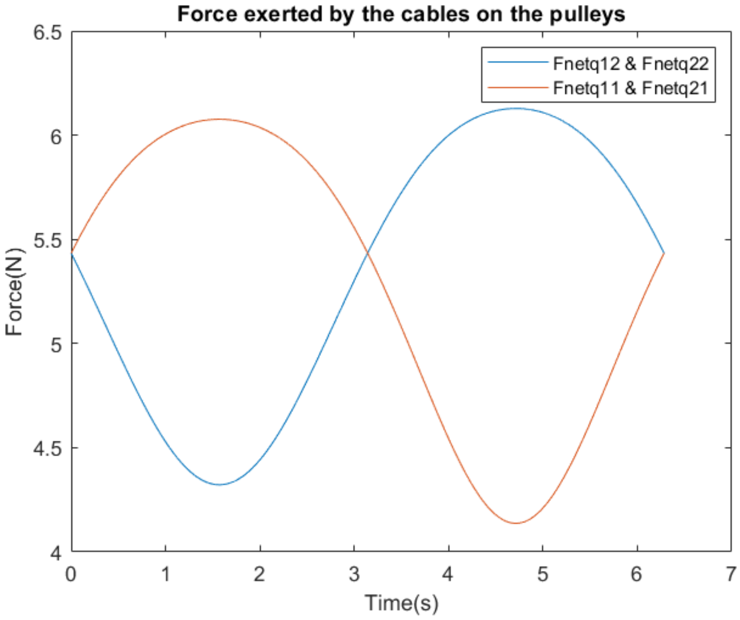

Figure 3.5: Net forces acting on DOFs (pulleys) with respect to time.

By perfect coupling we mean a lossless system in this case which is 100% efficient. The forces need to be counteracted in order to keep the system energy efficient otherwise there will be a requirement of additional power at the input to drive the system. As for a lossless system there needs to be net zero force when the system is in motion, which means no power is lost to the environment. But since perfect coupling is difficult to be implemented in the real world due to losses in the system such as friction, mechanisms such as compensation springs may be used to counter these probable losses. Compensation springs will allow the absorption and release of energy during the to and fro motion of the DOFs. As the DOFs move outward from the away from the springs attached to them, and move against the frictional forces, the springs will stretch and release the stored energy that will allow the DOFs to move against this frictional force. Again when the DOFs retreat towards the springs, they will compress allowing the absorption of energy to take place. In doing so the springs provide a force equal and opposite to the frictional force which helps in achieving an ideally lossless system.

The losses in the existing system are due to friction between the rack and pinion and the loss due to the heating of the motors. When the motors are removed and the mechanical coupling is realised, the losses as a result of friction will occur due to the rolling and sliding of the mechanical components in the system. Due to the displacement of the DOFs there will be a loss of power as a result of the frictional forces causing reduction in the efficiency. Hence, as mentioned above there might be requirement of some additional devices to reduce such losses.

The plot in 3.5 represents the magnitude of the forces with time and the maximum force that is caused due to spring elongation. The losses will be proportional to these forces that can be statically balanced with the help of springs. Since static balancing employs springs to counteract forces, the force on the system should be a function of the displacement of the DOFs and not time. It is therefore essential to parameterise the forces over the absolute position of the DOFs (i.e. $F \propto q$). This can be seen in Figure 3.6. For each point on each of the force plots with respect to the distances (q_{ij}, where $i, j \in \{1,2\}$), the stiffness of the spring can be computed, $K = \frac{\partial F}{\partial q}$. As seen in Figure 3.6, the curves are slightly non-linear in nature when compared to a linear curve and hence a linear spring cannot be utilized to follow such behaviour. In order statically balance the system in a perfect manner the non-linear behaviour of the forces has to be reproduced. This can essentially be done in two ways:

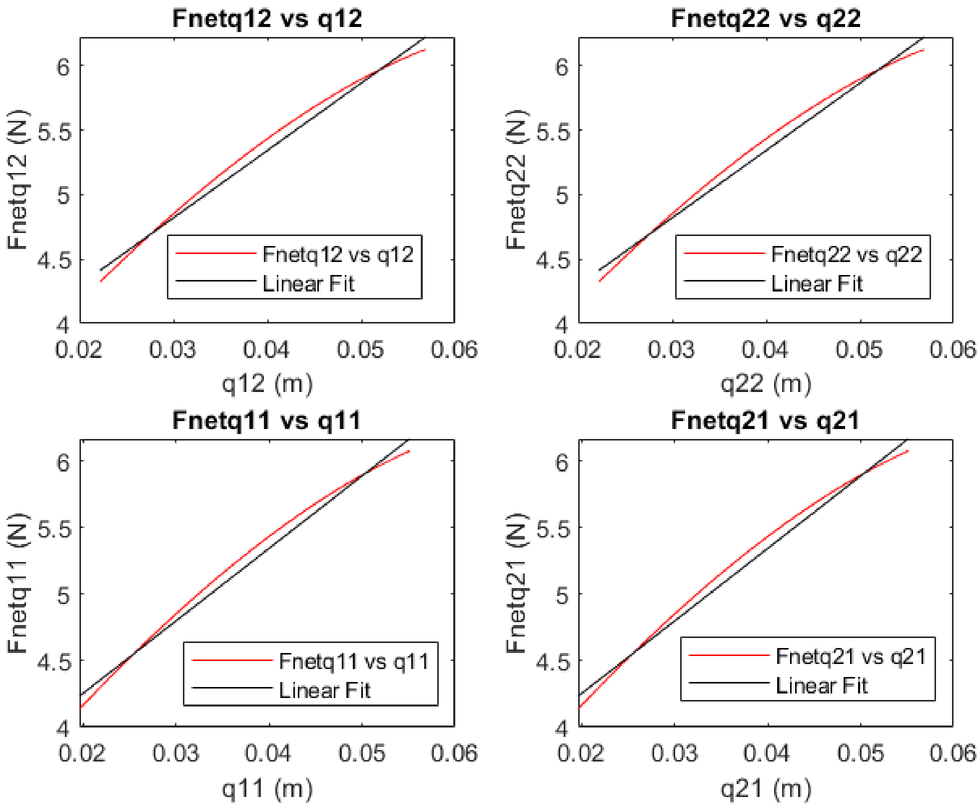

Figure 3.6: Force with respect to change in position of DOF and their corresponding linear fits.

- Either a non-linear spring has to be designed as such that it fits the requirements.
- Or a linear spring has to driven in such a way that its displacement replicates the trajectory of $\boldsymbol{q}$, for example forcing it along a spiral.

In order to execute the second method, a motion mechanism can be implemented using a linear spring which makes the deflection non-linear. Since the non-linearity is not really large in comparison to a linear fit, it is possible to implement such a technique using a cam profile. This is further discussed in section 4.2.2.

3.4 Flow of Energy

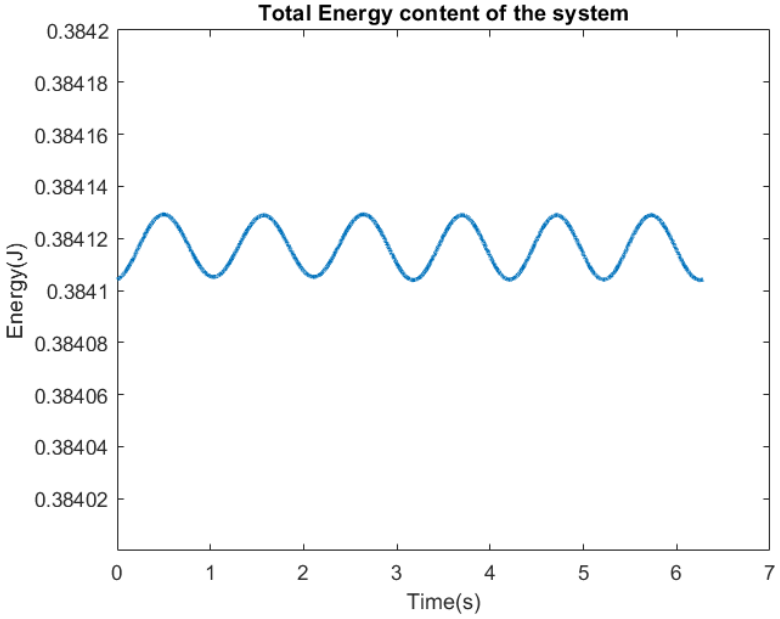

Figure 3.7: Total energy contained in the system over a period of time which is relatively constant.

Energy efficiency is an important criteria in robotic applications. For a system to be energy efficient the total output power must be close to the total input power. This is always not possible in a non-ideal scenario where there are losses such as friction. However for devices such as VSAs the power supplied must be employed for doing useful work at the actuator output and not to change the apparent output stiffness. This means that it should be feasible to change the apparent output stiffness of the actuator without the injection or extraction of energy to and from the elastic elements (Visser et al. (2011)).

A theoretical power analysis has been developed to verify the energy efficiency of the existing system. The total power in the system is derived from the energy and has been presented in the following subsection.

3.4.1 Total Power present in the system

The total energy content of the system as mentioned in equation 3.4 should remain constant for an energy efficient system (Figure 3.7) [3]. Keeping this in mind the time derivative of the energy was calculated which resulted in the total power of the system. Since the energy content of the system is constant, the rate of change of energy which is power should result in zero. This can be expressed as:

$$\frac{dH(s)}{dt} = k_1(L_1(\boldsymbol{q},\theta) - \overline{L_1})\frac{d}{dt}(L_1(\boldsymbol{q},\theta)) + k_2(L_2(\boldsymbol{q},\theta) - \overline{L_2})\frac{d}{dt}(L_2(\boldsymbol{q},\theta)) \tag{3.23}$$

$$\text{Therefore,} P_{\text{total}} = F_1\dot{L}_1(\boldsymbol{q},\dot{\boldsymbol{q}},\theta) + F_2\dot{L}_2(\boldsymbol{q},\dot{\boldsymbol{q}},\theta) \tag{3.24}$$

---

[3] The sinusoidal waveform of the energy content is due to the periodic nature of the forces in the system. But since the variations in the amplitude are minuscule, the energy system can be approximated to be constant over time. The maximum change with respect to the average value of the energy was calculated to be 0.0033%.

where,

$$\dot{L}_1(\boldsymbol{q},\dot{\boldsymbol{q}},\theta) = \\ \frac{d}{dt}(L_1(\boldsymbol{q},\theta)) = \frac{q_{11}\dot{q}_{11}}{\sqrt{c_1^2+q_{11}^2}} + \frac{(q_{11}+q_{12})(\dot{q}_{11}+\dot{q}_{12})}{\sqrt{b_1^2+(q_{11}+q_{12})^2}} + \frac{\dot{q}_{12}(d_\theta\cos\theta - l_\theta + q_{12})}{\sqrt{(a_1 - l_\theta\sin\theta)^2+(d_\theta\cos\theta - l_\theta+q_{12})^2}} \tag{3.25}$$

$$\dot{L}_2(\boldsymbol{q},\dot{\boldsymbol{q}},\theta) = \\ \frac{d}{dt}(L_2(\boldsymbol{q},\theta)) = \frac{q_{21}\dot{q}_{21}}{\sqrt{c_2^2+q_{21}^2}} + \frac{(q_{21}+q_{22})(\dot{q}_{21}+\dot{q}_{22})}{\sqrt{b_2^2+(q_{21}+q_{22})^2}} + \frac{\dot{q}_{22}(d_\theta\cos\theta - l_\theta + q_{22})}{\sqrt{(a_2 + l_\theta\sin\theta)^2+(d_\theta\cos\theta - l_\theta+q_{22})^2}} \tag{3.26}$$

F_1 and F_2 are the forces due to the elongation of the springs k_1 and k_2 respectively (refer to Equation 3.15).

The total power (P_{total}) in the system was calculated from the above equations and was found to be in the order of 10^{-5} which is close to zero. The residual error is due to the Fourier approximation of the $\boldsymbol{q}$ trajectories. The DOF motions were computed to ensure zero change in energy content, therefore this result is expected and by construction. Hence this result confirms achievement of the design goal of changing stiffness without changing energy content i.e. $\frac{dH(s)}{dt} = 0$. It affirms that since the total energy content of the system remains unchanged, the rate of change of energy which is power will be zero. This is indicated in Figure 3.8 which shows the change in power in the system which is constant when plotted over time.

The above calculations are done keeping the value of $\theta = 0$. If θ was a non-zero value, the equilibrium position of the system would change due to the deflection of the output bar. During such a state it is unpredictable as to how the system will behave since its energy content would change. This would mean that changing the stiffness in a deflected state without changing the equilibrium position would require $\frac{dH(s)}{dt} \neq 0$. The DOF trajectories need to be recomputed if θ was a non-zero value, and it would change accordingly if θ was changing. This indicates that for a certain stiffness change configuration, there maybe different DOF trajectories i.e. different $\boldsymbol{q}$ values for different values of θ. This would make the system more complex, hence, $\theta = 0$ was chosen to simplify the calculations.

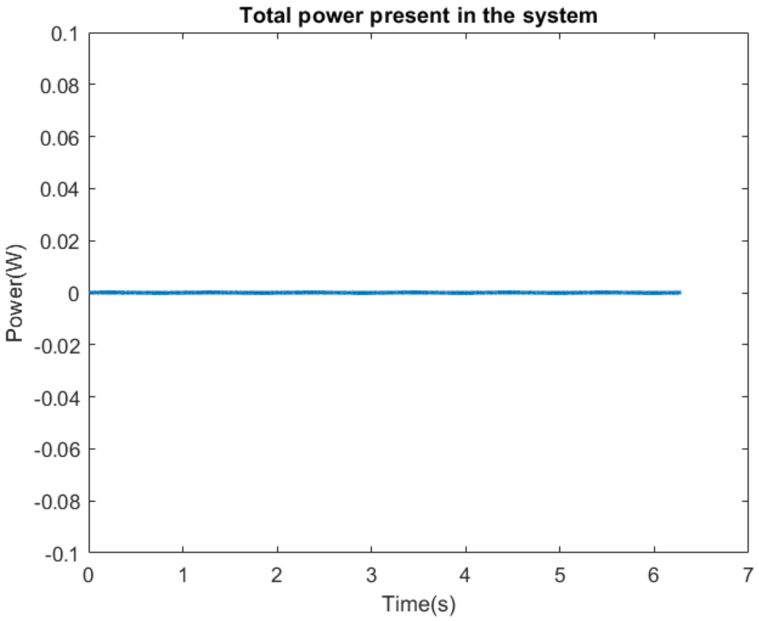

Figure 3.8: Total power content in the system obtained from $\frac{dH(s)}{dt}$=0.

3.4.2 Use of compensation springs

The next case is the use of the force compensation springs in the system. The forces computed in 3.16 and 3.17 which are a result of the extension of the tendon lengths are identical to these kinematically obtained expressions as represented Equations 3.29 to 3.32. As a result if there would be no coupling, springs could be introduced to compensate these forces acting on the DOFs. This indicates that the net zero force will have a spring compensation that generates equal force but opposite in direction for each configuration. These force expressions are essential to show the flow of energy generated as a result of the force from the springs k_1 and k_2.

$$F(\boldsymbol{q},\theta) = \frac{\partial H(s)}{\partial \boldsymbol{q}} \tag{3.27}$$

$$F(\boldsymbol{q},\theta) = k_1(L_1(\boldsymbol{q},\theta) - \overline{L_1})\frac{\partial L_1(\boldsymbol{q},\theta)}{\partial \boldsymbol{q}} + k_2(L_2(\boldsymbol{q},\theta) - \overline{L_2})\frac{\partial L_2(\boldsymbol{q},\theta)}{\partial \boldsymbol{q}} \tag{3.28}$$

The forces on DOFs q_{11} and q_{12} are dependent only on the energy stored in the elastic element k_1. Similarly the forces on DOFs q_{21} and q_{22} are dependent on k_2. This is due to the output link being fixed, i.e. $\theta = 0$. Hence their respective force equations will be as follows:

$$\begin{aligned}
F_{q_{11}} &= k_1(L_1(q_{11},\theta) - \overline{L_1})\frac{\partial L_1(q_{11},\theta)}{\partial q_{11}} \\
&= k_1(L_1(q_{11},\theta) - \overline{L_1})\left(\frac{q_{11}}{\sqrt{q_{11}^2 + c_1^2}} + \frac{q_{11}+q_{12}}{\sqrt{b_1^2 + (q_{11}+q_{12})^2}}\right) \qquad (3.29)\\
F_{q_{12}} &= k_1(L_1(q_{12},\theta) - \overline{L_1})\frac{\partial L_1(q_{12},\theta)}{\partial q_{12}} \\
&= k_1(L_1(q_{12},\theta) - \overline{L_1})\left(\frac{q_{11}+q_{12}}{\sqrt{b_1^2 + (q_{11}+q_{12})^2}} + \frac{d_\theta \cos\theta - l_\theta + q_{12}}{\sqrt{(a_1 - l_\theta \sin\theta)^2 + (d_\theta \cos\theta - l_\theta + q_{12})^2}}\right) \qquad (3.30)\\
F_{q_{21}} &= k_2(L_2(q_{21},\theta) - \overline{L_2})\frac{\partial L_2(q_{21},\theta)}{\partial q_{21}} \\
&= k_2(L_2(q_{21},\theta) - \overline{L_2})\left(\frac{q_{21}+q_{22}}{\sqrt{b_1^2 + (q_{21}+q_{22})^2}} + \frac{d_\theta \cos\theta - l_\theta + q_{22}}{\sqrt{(a_2 + l_\theta \sin\theta)^2 + (d_\theta \cos\theta - l_\theta + q_{22})^2}}\right) \qquad (3.31)\\
F_{q_{22}} &= k_2(L_2(q_{22},\theta) - \overline{L_2})\frac{\partial L_2(q_{22},\theta)}{\partial q_{22}} \\
&= k_2(L_2(q_{22},\theta) - \overline{L_2})\left(\frac{q_{21}}{\sqrt{q_{21}^2 + c_2^2}} + \frac{q_{21}+q_{22}}{\sqrt{b_2^2 + (q_{21}+q_{22})^2}}\right) \qquad (3.32)
\end{aligned}$$

The forces computed from the equations are equal to each other for the DOFs in both the top and the bottom halves respectively as expected due to symmetry around $\theta = 0$. The change in the energy content as seen in the previous section was evaluated to be zero which means the forces balance each other out when the DOFs are coupled around this configuration. Since such a circumstance occurs, it can hence be concluded that the compensation springs in this case aren't necessary for counteracting the internal forces. This means theoretically the coupling is perfect and no additional compensation mechanisms are required. However, as previously discussed, compensation springs might be necessary to reduce the losses that would occur in the system due to friction. It is to be noted that if we would not couple the DOFs and keep the four separate motors, then the force compensation springs will reduce the individual powers required from these motors. Springs will significantly help in mitigating the losses and help compensate the internal forces along with the motor.

3.4.3 Power, Work Done and Efficiency

In order to establish the energy efficiency of the system, the power injected into each of the DOFs were calculated and their sum total were checked if they were close to zero or not. This can be represented as the product of the internal forces F_q and velocity $\dot{\boldsymbol{q}}$ of the DOF:

$$P_q = F_q \cdot \dot{\boldsymbol{q}} \qquad (3.33)$$

This graphical representation of the individual powers acting on each of the the four actuated DOFs can be seen in Figure 3.9. The power acting on each of the DOFs P_q that was found was a function of time t.

The individual power of the DOFs is non-zero. Theoretically the sum total of these values should be zero i.e. $\Sigma P_q = 0$, which it was found to be for this system as seen in Figure 3.10, since the total power flowing into the system must be equal to the total output power. This is due to construction as the total energy content cannot change.

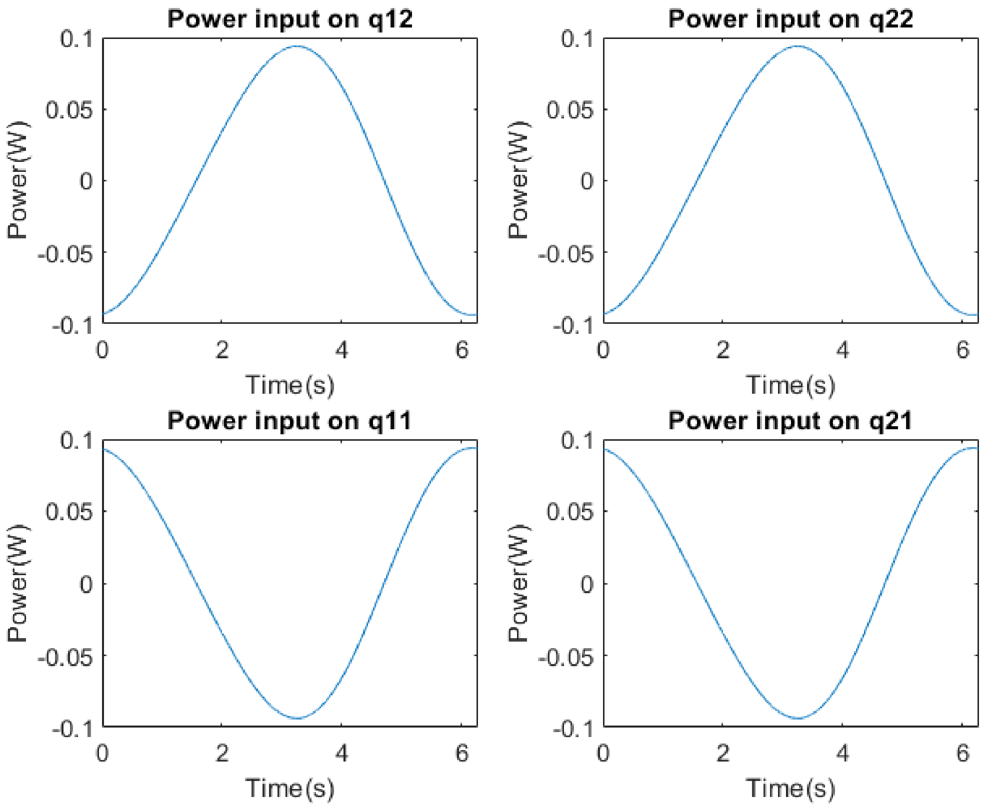

Figure 3.9: Power input into each of the four actuated DOFs in the VSA.

The work done $W(\boldsymbol{q},\theta)$ on the individual DOFs can be calculated as the integral of the power (P_q) over time. This can also be defined as the integral of the product of the force acting on the DOFs due to the springs over a time period from 0 to T and the velocity $\dot{q}$, formulated as:

$$W(\boldsymbol{q},\theta) = \int_0^T P_q(t)dt = \int_0^T F_q(\boldsymbol{q}(t),\theta(t))\dot{\boldsymbol{q}}(\boldsymbol{t})dt \tag{3.34}$$

Since the force is variable, we need to compute the work done by a variable force over a displacement q of a DOF. The work done by a force over a relative displacement can then be denoted as:

$$W(\boldsymbol{q},\theta) = \int_{q(t=0)}^{q(t=T)} F_q(\boldsymbol{q}(t),\theta(t))dq \tag{3.35}$$

The trapezoidal rule was used to compute the individual work done by finding the area under the curve. The trapezoidal rule finds the area under the curve for a by approximating the region. Since both the force and the displacement of the DOFs were varying, it could not be integrated without normalising the force. The error was calculated for this rule and was found to be of the order 10^{-9}, which means the values obtained through this method were highly accurate. The sum total of the individual work done by the DOFs was effectively found to be zero.

As the total power in the system under the condition of $\theta = 0$ was found to be zero ($\frac{dH(s)}{dt} = 0$), changing the stiffness requires zero power. This should hold true if in the proposed system, the DOFs are coupled. With perfect coupling the above condition where total work done is zero and zero input power can be achieved. Then as a result the force compensation springs will not be of any use. However, as mentioned previously in section 3.3, perfect coupling occurs only in ideal conditions as in the real world the system would face losses due to friction. There-

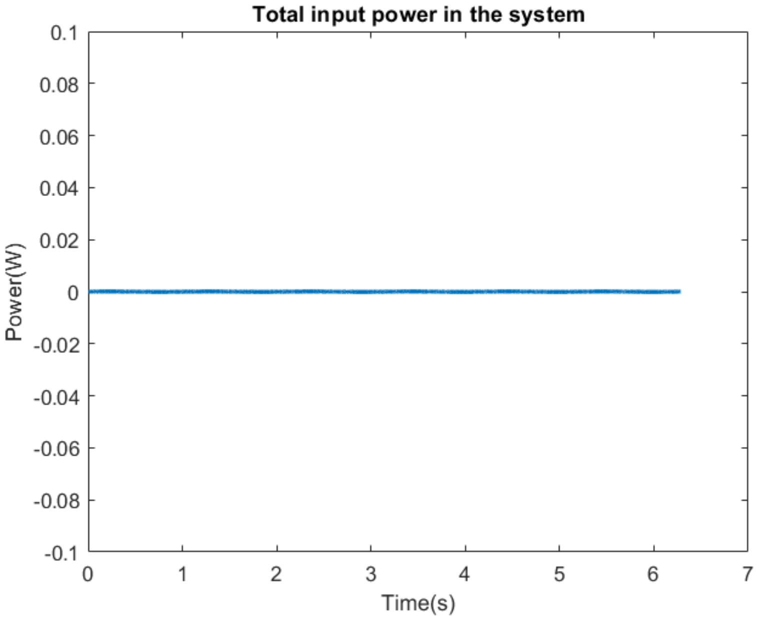

Figure 3.10: Total power injection into the VSA through the control port with respect to time.

fore compensation springs will help reduce the losses thereby making the system more energy efficient.

To make an estimate of the losses after coupling the system, a black-box model has been established. It is a black-box model since we are not sure what kind of system it will be other than the fact there will be periodic movement of the actuators based on some rotational input with some phase angle. Let F_{losses} be the force on the DOFs due to the various losses in the system and F_{comp} be the spring compensation force. Considering that F_{losses} is dependent on the forces F_q and friction to be the only factor that contributes to these losses, they can be computed as (Van Geffen (2009)):

$$F_{\text{losses}} = \mu F_q \cos(t)\text{sign}(\dot{q}) \tag{3.36}$$

The value of μ is the frictional constant between two surfaces, in this case polyoxymethylene (POM) and steel and was found to be 0.14 (Tri (2020))). The force, $F_q \cos(t)$, is the the normal force exerted by the surfaces on each other, which varies non-linearly due to the to and fro movement of the DOF in the left and the right direction for a certain time period from 0 to 2π. The value of $\text{sign}(\dot{q})$ represents the dependence of the force due to losses on the DOF's velocity.

In such circumstances the compensation springs will mitigate these losses such that $P_{\text{control}} = 0$ i.e. $F_{\text{comp}} + F_{\text{losses}} = 0$. Otherwise injection of power at the input will be a requirement for actuating the DOFs. Friction is deemed as the biggest contributor to losses in the case of the proposed system. Hence a friction model has been derived in order to estimate its effect and the contribution of the compensation springs in section 4.3. However it is just an estimate and due to the nature of friction, there may be cases where the forces are out of bounds of the minimum and maximum expected force and the springs are not able to compensate any further.

The efficiency (η) at each DOF of the system can be found out by calculating their individual power loss (P_{losses}) which can be formulated as:

$$P_{\text{losses}} = F_{\text{losses}} \cdot \dot{q} \tag{3.37}$$

The efficiency (η) (as %) can then be calculated as:

$$\eta = \frac{\text{Power Output}}{\text{Power Input}} \times 100 \tag{3.38}$$

$$\eta = \frac{P_q}{P_q + P_{\text{losses}}} \times 100 \tag{3.39}$$

The above calculation was done for the new proposed system with coupled DOFs assuming the system is completely mechanical. The losses occur as a result of the movement of the DOFs as they slide against some surface when actuated by some mechanical input. In case of the existing system mentioned in Groothuis et al. (2020), it is electromechanical due to the servomotors present for actuating the DOFs. In that case the losses will also include the heating losses due to resistance in the armature.

From the values that were obtained, the estimated losses and the efficiency for the new system were calculated. The comparison of the input power with the losses is illustrated in the plots in Figure 3.11. The results of the calculated power loss from the next chapter will be compared with these plots.

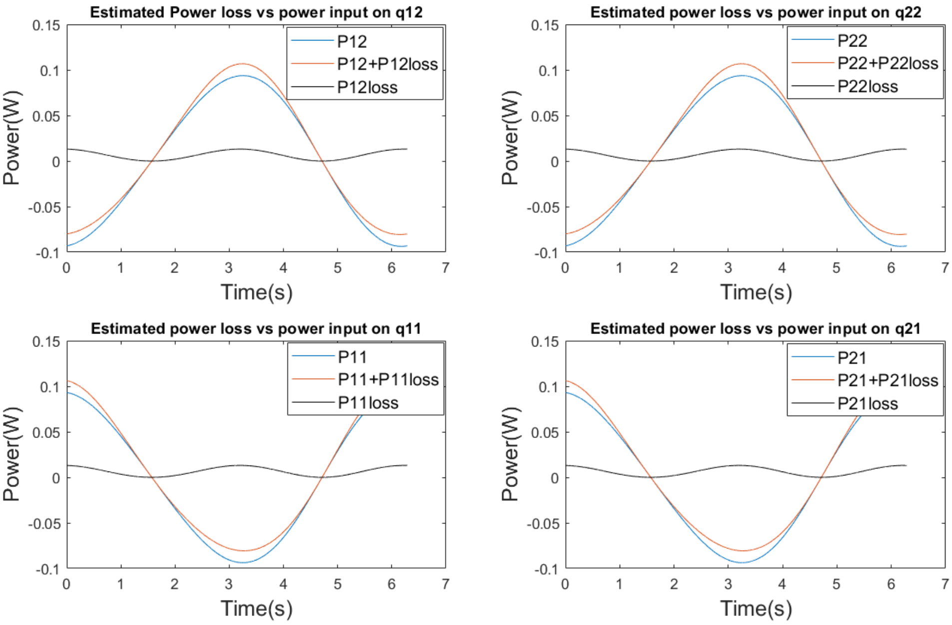

Figure 3.11: Estimated power loss in the DOFs for the new system. Comparison between input power (Pij), input power with losses(Pij+Pijloss) and the power loss(Pijloss), where i,j $\in \{1,2\}$.

The efficiency plots are shown in Figure 3.12. It shows the increase in efficiency up until a point where there is no input power on the DOFs and then again drops when the DOFs start returning to their initial configuration. This repeats for every cycle. This is due to their periodic to and fro motion of the DOFs over a time period of 0 to 2π. The mean efficiency (η) over the period of time corresponding to all the DOFs was calculated to be 91.96%. The efficiency calculations are an essential foundation for defining the results of the friction model. It is to be seen how much these values deviate or the plots behave in comparison to these estimated results when the synthesis for the new system along with the friction calculation is done in the next chapter.

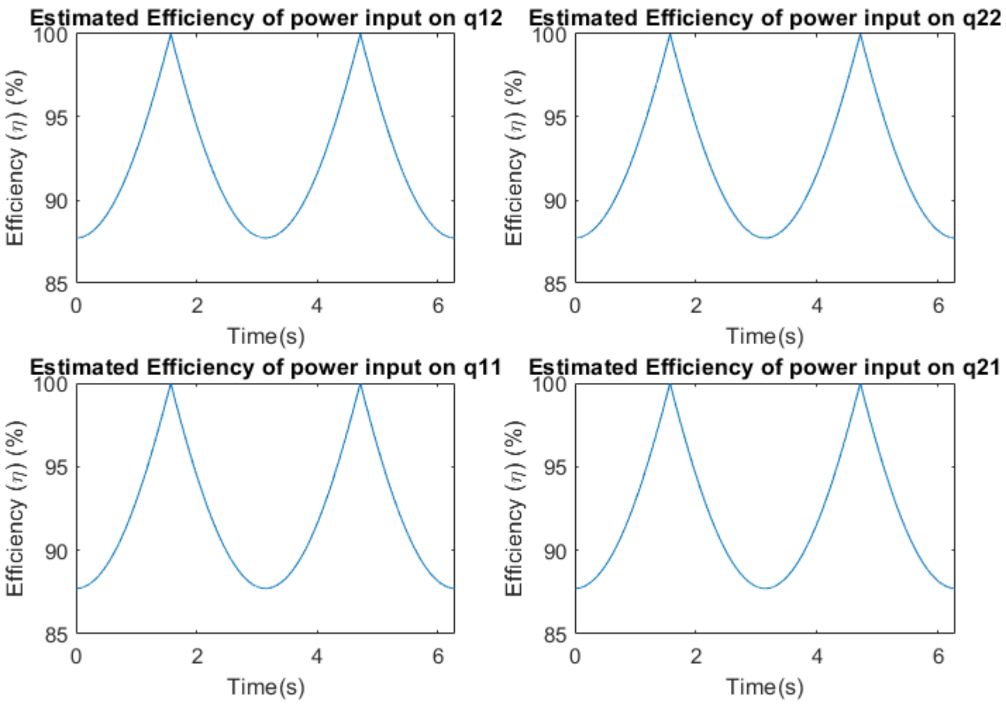

Figure 3.12: Estimated Efficiency of the power input on the DOFs for the new system.

3.5 From Analysis to Synthesis

From this chapter it was deduced that hypothetically the four DOF system can be made more compact by coupling the actuated DOFs. Therefore a mechanism has to be designed that realizes the specific motions that follows the equation 3.12 or in particular the trajectory of the motions as seen in Figure 3.2. The individual motors are removed when the DOFs are coupled. If the coupling is perfect then there is no requirement for any additional mechanisms as the internal forces will be balanced out. However, due to the losses in any physical system, force compensation springs maybe required to nullify them. The force equations 3.16 and 3.17 can help design springs that generates reaction forces to reduce these losses. So compensation springs will be used to improve the efficiency of the system. As shown in the plots in Figure 3.11, there is some additional power required at the input to actuate the DOFs. This means that energy is required at the input to do work against the losses. The use of compensation springs can help mitigate this by storing and releasing energy to work against the losses. The calculations can be verified to this estimate after the friction model is developed in the next chapter to understand whether the assumptions made were correct or not.

It is to be noted that coupling the DOFs would necessarily mean that the modes of operation of the system will be limited. This means that the equilibrium position of the system cannot be changed. There will be only one mode of operation present, i.e. changing the stiffness.

The results in this Chapter define the trajectories of the DOFs that need to be executed and coupled so a single, reduced DOF model, can be manifested. Hence it enables us to define the parameters of the new mechanism.

4 Synthesis of DOF Reduction

To realize a physical model for the reduced DOF system, it is essential to analyse how the motion trajectories can be reproduced mechanically. In order to achieve that goal, a brief introduction of straight line mechanisms that could have been possibly implemented will be explored in order to get an idea to build the system. The major drawbacks of these conventional systems will be discussed and a new system altogether will be proposed comprising of spirals, cam profiles and grooves. Springs will be introduced for compensating the losses that were discussed in the previous chapter. A theoretical friction model of the system will be established which will be compared to the estimated model in the previous chapter. Along with these, the efficiency of the system will also be verified with the estimate and the effectiveness of the springs to negate the losses will be studied.

4.1 Straight Line Motion Mechanisms

A variety of motion mechanisms exist which convert a rotation to a straight line motion. Some examples are the slider crank mechanism, Cardan gear mechanism and hypocycloid mechanism. The slider crank uses a simple rotational disk or gear that drives a shaft connected to a piston producing a harmonic output with some constant additional terms. The Cardan gear mechanism comprise of sun and planet gear with the latter having a diameter half of the former. The planet gear is connected to a secondary planet gear of equal diameter. A link runs from the centre of the sun gear to the centre of the secondary planet gear. There is another link or shaft attached to the secondary planet gear that therefore follows a straight line motion when all the gears are actuated.

The hypocycloid mechanism is similar to the Cardan in terms of operation, the difference lies in the fact that it consists of a ring gear and an inner planet gear with a diameter of half of the ring gear. The approach has already been implemented for the construction of a rotational VSA (Groothuis et al. (2012), Groothuis et al. (2013)), essentially for conversion of rotational to linear motion. Even though the straight line motion can be reciprocated from such mechanisms, they are mostly simple harmonic in nature and therefore are not able to reproduce the identical motion that is required as mentioned in Equation 3.12.

$$q = a_0 + a_2 \cos(t) + a_4 \cos(4t) + b_1 \sin(t) + b_3 \sin(3t) + b_5 \sin(5t)$$

Unless the aforementioned trajectory is reproduced the stiffness profile of the system will no more be the desired one and will be effect to change as a result of the alterations in the motion profile.

In order to obtain the correct trajectory along with reducing the actuated DOFs, we proposed spirals that would be grooved onto the wheels/gears to replicate the motion of the pulleys as in the current system. The spirals can be defined as the polar plots obtained from the Cartesian coordinates of the q trajectories obtained in Equations 3.13 and 3.14 for the bottom and the top pulleys respectively. Pins can act as the DOFs as a substitute to the pulleys. These pins can be placed at the junction of horizontal straight grooves (carved on a flat plate, placed on top of the wheels/gears) and the spiral grooves carved out on a rotating gear/wheel. These will produce periodic straight line motions with trajectories identical to aforementioned q trajectories. This proposed mechanism is further elaborated in the next section.

4.2 System Design

Since the conventional straight line motion mechanisms could not be implemented to replicate the present system, a different approach was required to reproduce the results of the four DOF system. The system design of this comprises of four major parts in particular namely: Motion

Spirals, Force Spirals (which are cut on wheels/gears), Straight Grooves that limit the motion of the pin to a linear motion and the Pin which will be the actuated DOF for the system. But before that it is important to have a brief discussion on the drawbacks and advantages of reducing the DOFs. The aim of the project is to reduce the actuated DOFs to less than or equal to two. With

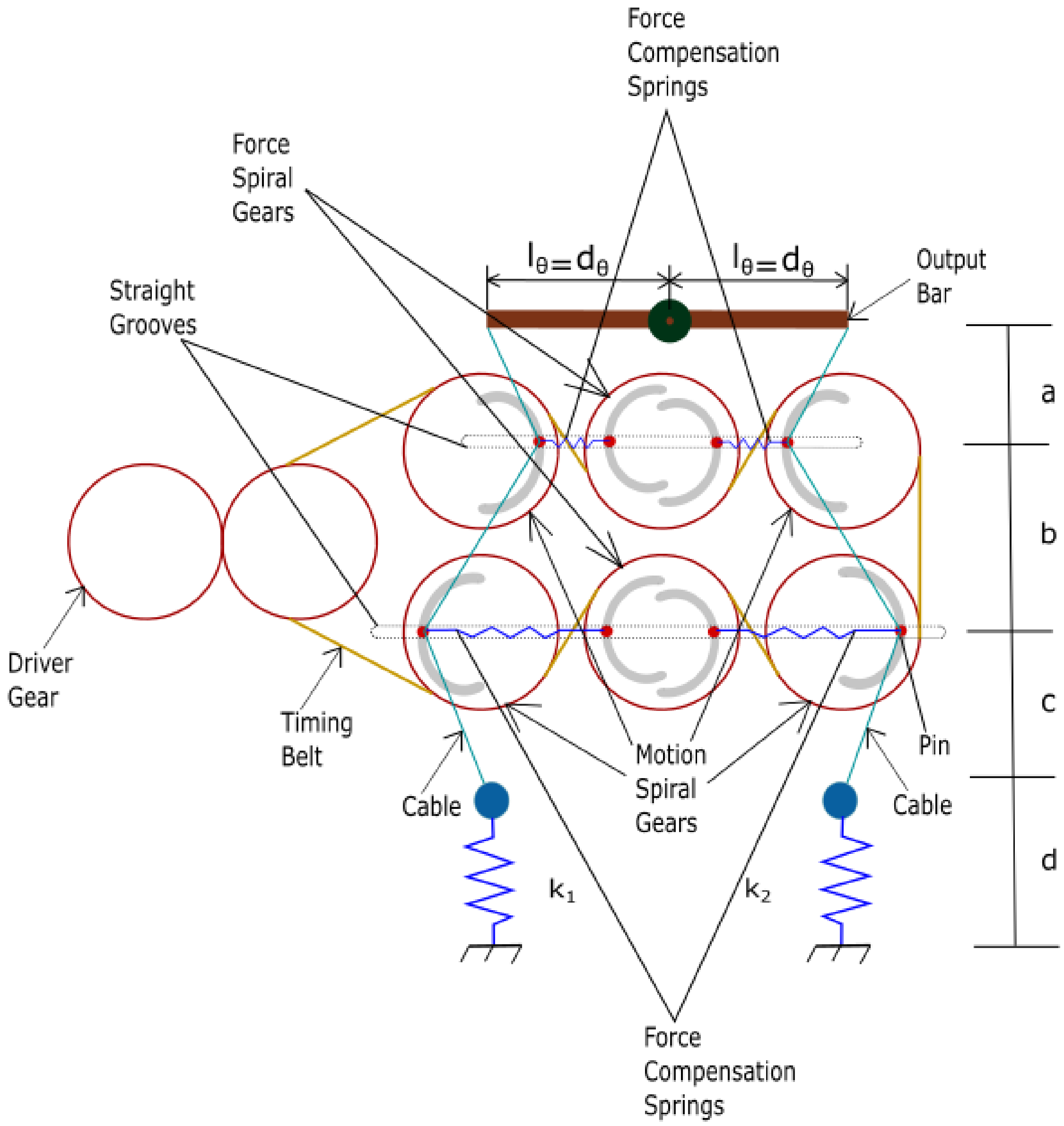

Figure 4.1: New Proposed VSA design with reduced actuated DOFs.

two DOFs, there would be two motors involved in the setup. In a traditional VSA, the advantage of having two motors is that one is used to control the stiffness, whereas other controls the position. Reducing this to one DOF will therefore not provide independent control over the two parameters. Also for the system at hand, the two motors would allow the individual control of the left and the right limbs. This means that actuating the pulleys (DOFs) q_{11} and q_{21} only would be possible without disturbing the pulleys (DOFs) q_{12} and q_{22} and also the vice versa. Obtaining such a behaviour from just one motor is not possible, as it will actuate all the DOFs simultaneously. Since the primary goal is to inspect whether the coupling of the DOFs and compensation of forces are possible in the system, only one DOF will suffice for the time being. In order to do so, the motion of the pulleys (DOFs) must be such that they have trajectories that are identical to the ones that were obtained from the already existing system as seen in Figure 3.2.

A schematic diagram of the proposed system with its various components has been presented in Figure 4.1. It contains the wheels/gears with the spirals. The straight grooves and the pins are also indicated along with it. The straight grooves (as shown in Figure 4.1) are present to limit the movement of the DOF to a straight line motion that follows the trajectories obtained from the system presented in Groothuis et al. (2020). These grooves can be cut on a flat plate which is to placed on the top and bottom of the setup. A straight (horizontal) groove is positioned at the junction of the spiral groove end and the DOF is fit into it. When the wheels/gears containing the spiral groove rotates, the straight groove restricts the motion of the DOF and only allows a linear to and fro motion of a periodic nature based on the configuration of the spiral, providing a motion profile identical to the ones in Figure 3.2.

In the case of the new system, the DOF is a pin that would be actuated due to the rotation of the wheels/gears. These pins will be placed at the junction of the spirals and the straight grooves to move along the desired trajectory. The stiff cables attached to the horizontal (output) bar will be connected to the pins both on the left and right side of the system as seen in the Figure 4.1. Forces act upon these pins due to the elastic elements (springs k_1 and k_2) through the cables which are required to be compensated. Therefore these pins will also act as the attachment points for the springs between the force and motion spirals for force compensation and will act accordingly to counteract the forces. Since in our case the system by construction compensates the internal forces, the springs will be used to mitigate the losses due to friction.

It is to be noted that the length of the straight grooves should be long enough for the pulley to traverse, which is atleast equal to the difference between the maximum and the minimum positions along which the pins (DOFs) move. Although it is always safer to keep them longer. The width of the straight grooves is (equal to the width of the spirals) dependent on the dimension of the pin (DOF) to which the cable is attached.

The wheels/gears for the force and motion spirals will be connected to each other with the help of a timing belt. These will be driven by an input wheel/gear with the help of a hand crank, that will act as a rotational input, which is the single actuated DOF in the newly designed system. The actuation of the rotational input will enable the other parts of the setup to actuate simultaneously to obtain the desired behaviour.

Thus, such a mechanism was chosen over the previous straight line motions as it would keep the stiffness profile intact and also fulfill the objectives. The parametric design of these spirals are further discussed in the following subsections.

4.2.1 Definition of Motion Spirals

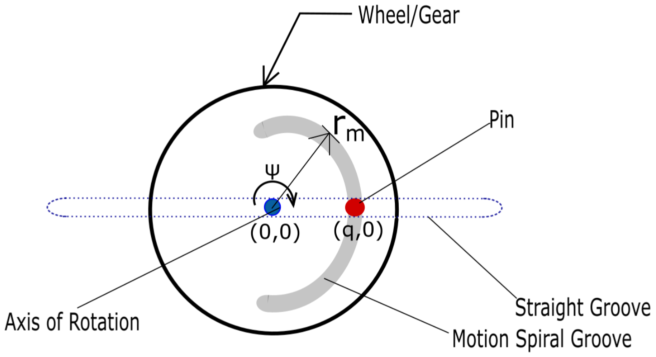

Figure 4.2: Schematic diagram of a proposed Motion Spiral groove on a wheel/gear.

In Figure 4.2, a wheel/gear can be observed with a groove cut out in the shape of a spiral with a particular thickness. The spiral is plotted on the x-y coordinate from $\psi = -\pi/2$ to $\pi/2$ with the centre of the wheel located at the origin. It is oriented in such a way that the pin is situated at $(q, 0)$ away from the centre. This is a physical representation of a motion spiral with the straight groove and the pin.

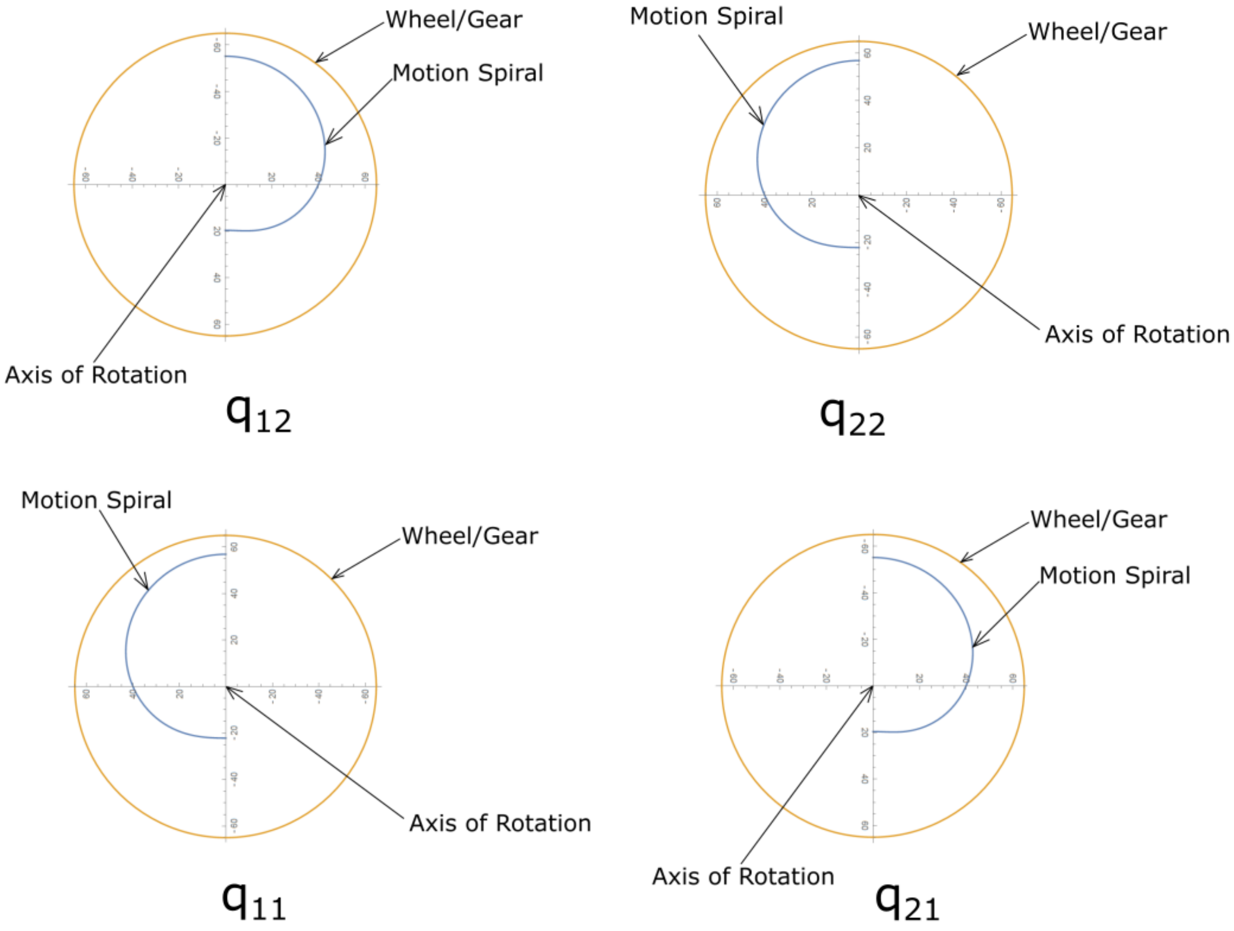

Figure 4.3: Motion Spirals obtained from the polar coordinates of the $\boldsymbol{q}$ trajectories. The dimension of the coordinates are in mm.

The motion spirals (Figure 4.3) are to be used as a substitute mechanism for obtaining the motion profiles in place of the linear motors. They are supposed to carved onto gears or wheels in the form of grooves. In order to appropriately get the correct trajectory, the polar coordinates of the trajectories were calculated. The trajectories are symmetric, which means that only half of a spiral on a wheel/gear needs to be created to get the entire motion. For obtaining a single DOF, a rotational input will be used with a certain angle of rotation ψ. It is to be coupled to some transmission elements that would give us the desired output of the various elements of $\boldsymbol{q}$. The equations of the x and y coordinates of the motion spiral are given by with respect to the input angle ψ:

$$x_m = r_m(\psi)\cos\psi \tag{4.1}$$

$$y_m = r_m(\psi)\sin\psi \tag{4.2}$$

Such that the configuration of each DOF q_{ij} is given by the radius of its corresponding motion wheel $r_{m_{ij}}$ at the current input angle ψ. The radius of the wheel/gear is determined by the largest value of r_m and should be $> r_m$ to properly fit onto it leaving some space at the edges.

As a result of the rotation of the input wheel the value of q will be a function of ψ and can be expressed as:

$$q(\psi) = a_0 + a_2\cos(\psi) + a_4\cos(4\psi) + b_1\sin(\psi) + b_3\sin(3\psi) + b_5\sin(5\psi) \tag{4.3}$$

What the motion spiral does is it creates a cam profile for the DOF (in this case a pin) to follow and is limited to a periodic to and fro motion in the x-axis which replicates the trajectories which are obtained in Figure 3.2 depending on which spiral the pin is located. There are many instances where the use of cam profiles to obtain a particular linear or rotational motion for VSAs were deemed useful such as Spagnuolo et al. (2017) and Sun et al. (2018). Hence this method was thought of in order to tackle the problem at hand.

4.2.2 Definition of Force Spirals

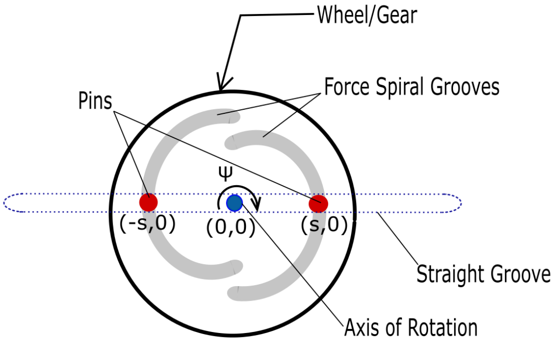

Figure 4.4: Schematic diagram of proposed Force Spiral grooves on a wheel/gear.

Similar to a motion spiral, a schematic representation of two force spirals on a single wheel/gear is shown in Figure 4.4 plotted from $\psi = -\pi/2$ to $\pi/2$. The center is located at the origin and the pins on either left and right spirals are located at $(-s, 0)$ and $(s, 0)$ respectively. The straight groove which restricts the pins to move in a horizontal direction is also indicated. The idea of having two force spirals on a single disc is to reduce the size of the hardware and is feasible due to the symmetry of the system.

In order to increase the efficiency of the system and reduce the losses, compensation springs were proposed to achieve this. As seen in Figure 3.6, the change in the forces acting on the DOFs with respect to their absolute position is slightly non-linear. Since the losses in the system due to friction are presumed to be proportional to these forces, springs can be used to reduce these losses. In theory, non-linear springs can be used for getting the identical profiles of these forces. But designing non-linear springs is difficult. Hence the force spirals in the aforementioned paragraph was proposed. The force spirals similar to the motion spirals can act as cam profiles to guide a linear spring along a non-linear path (Figure 4.5). One end of the linear spring will be attached to a pin at position q of a motion wheel, while the other end on a pin at position s of the force spiral (as seen in Figure 4.1). The elongation of the spring along the spiral with its end points attached to the positions q and s can help realize the non-linear force profile.

The internal forces present in the system can be written as a function of the input angle ψ, which is varied from 0 to π. Let K be a chosen spring constant value of a linear spring [1]. The maximum spring force will be equal to K times the difference between the position of the pins

---

[1] The value of K in this case was chosen to be 140 N/m based on the hardware specifications. The choice of K value is dependent on the force (F_0) at rest length of the spring (L_0) which was mentioned in the specification by the manufacturer. The minimum force to be compensated must be higher than the the force (F_0). It was found that any spring above 70 N/m would suffice, but 140 N/m was chosen because it would be the optimum size for our system.

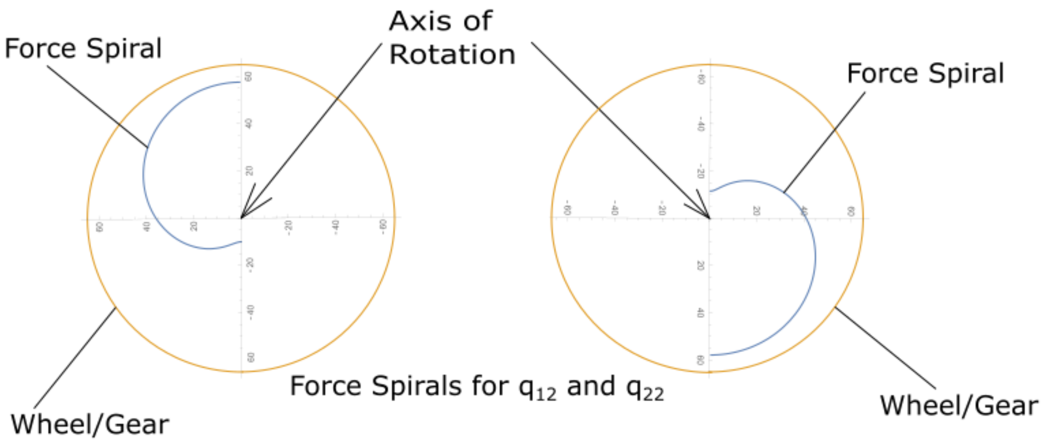

Force Spirals for q_{12} and q_{22}

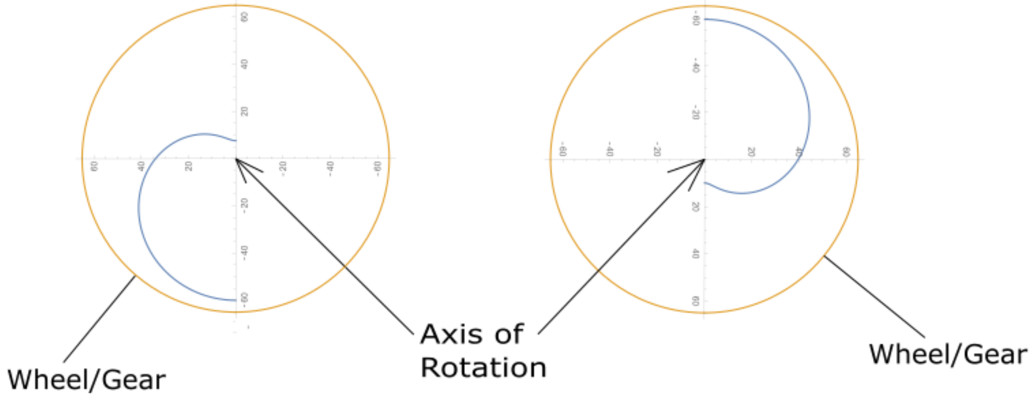

Force Spirals for q_{11} and q_{21}

Figure 4.5: Force Spirals obtained from the polar coordinates of the $s'(\psi)$ for the different $\boldsymbol{q}$ trajectories. The dimension of the coordinates are in mm. Of course two force spirals can be clubbed together into one wheel/gear as shown in Figure 4.4.

at q and s. The maximum force is the internal force F_q. The value of pin position s can therefore be determined from the following:

$$\begin{aligned} K(q(\psi)-s(\psi)) &= -F_q(\psi) && (4.4)\\ q(\psi)-s(\psi) &= -\frac{F_q(\psi)}{K} && (4.5)\\ s(\psi) &= q(\psi)+\frac{F_q(\psi)}{K} && (4.6)\end{aligned}$$

$s(\psi)$ is the position of the other end of the force compensation spring when the origin (zero position) of the coordinate system is considered to be the center of the motion spiral wheel. Since in the setup, all spirals wheels should be located at an optimum distance from each other, the shape of the force spiral needs to be taken and placed on a wheel/gear. After which the wheel/gear needs to be placed at a desired distance. In order to attach the springs on the pins (DOFs), there must be attachment points which will take up some space between the motion and force wheels/gears. This would result in having to place the force spirals at a position farther away from the center than the actual position, which means we need to provide an offset to the value of s. Then a contact point can be created on each of the pins located at s and q which would occupy the space created by the offset to attach the spring. This is to ensure the relative distance between the two points doesn't change. An offset is chosen as the distance from the center of the wheel to the shortest distance the force compensation pin has to move and is determined by the following:

$$s'(\psi) = s(\psi) - (\min(s(\psi)) - 0.01) \tag{4.7}$$

where $s'(\psi)$ is the relative distance from the center to the wheel to the shortest distance after applying an offset of 0.01.

The equations of the x and y coordinates of the force spiral are given by with respect to the input angle ψ, same as the one for the motion spirals:

$$x_f = s'(\psi)\cos\psi \tag{4.8}$$

$$y_f = s'(\psi)\sin\psi \tag{4.9}$$

Like the motion spirals, the radius of the wheels/gears for the force spirals is decided by the largest value of the s' and should be $> s'$.

4.3 Effect of Friction

The presence of friction affects the performance in mechanical systems. Even though the best efforts are made to keep them to minimum, it can never be completely negated. Since our new system is a completely mechanical system, friction plays a dominant role in the losses. Mitigation techniques such as using materials that cause less friction and smoothing the contact surfaces can be implemented to reduce these losses. However, to make the system energy efficient we have proposed the use of compensation springs to negate these losses.

A likely location in the system where a significant effect of friction can be witnessed is between the pins and the side walls of the spiral grooves on which they are placed. This section deals with the effect the friction plays on the output of the system. A theoretical analysis of the friction model is presented. The amount of extra work that is to be done to overcome these losses to obtain the desired output can also be expressed mathematically.

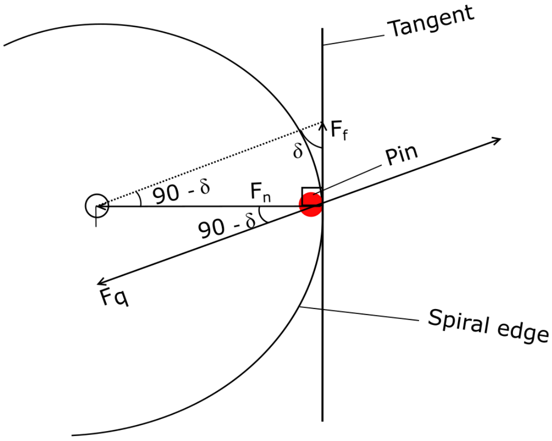

Figure 4.6: Depiction of Frictional force in the spirals

For the mathematical model to calculate the friction, we require the normal force (F_n) acting on the surface between the pin and the spiral. As the spiral will rotate, it will force the pin to change its position horizontally because it is restricted by the horizontal grooves. For every rotation there will be a relative amount of friction between the pin and the spiral walls that will contribute to some losses. For friction between the pins and the horizontal grooves, there will be a lot of factors of hardware specifications such as mass of the pins, the material used for the pins and the grooves and the area of contact between them. Therefore, they have been left out for the time being and briefly discussed in the next chapter. The system can be approximated such that the point where the pin touches the wall of the spiral can considered a line tangent to a curve which is the spiral (Figure 4.6). The frictional force (F_f) will act along this tangent. Finding the slope of the tangent drawn to the curve can help determine the angle of the sine component of the internal force on the DOF. This can be done using the polar coordinates of the motion spirals with respect to the rotation angle ψ. Hence, we can write the equations as the following:

$$x = q\cos\psi,\ y = q\sin\psi \tag{4.10}$$

q being the distance from center of the wheel/gear to the center of the spiral.

Therefore, the slope of the tangent is given by

$$\frac{dx}{d\psi} = \dot{q}\cos\psi - q\sin\psi \tag{4.11}$$

$$\frac{dy}{d\psi} = \dot{q}\sin\psi + q\cos\psi \tag{4.12}$$

$$\frac{dy}{dx} = \frac{\dot{q}\sin\psi + q\cos\psi}{\dot{q}\cos\psi - q\sin\psi} \tag{4.13}$$

For ψ = t, at ω = 1 rad/s

$$\frac{dy}{dx} = \frac{\dot{q}\sin t + q\cos t}{\dot{q}\cos t - q\sin t} \tag{4.14}$$

By definition, slope = $\tan\delta$, therefore,

$$\tan\delta = \frac{dy}{dx} \tag{4.15}$$

$$\tan\delta = \frac{\dot{q}\sin t + q\cos t}{\dot{q}\cos t - q\sin t} \tag{4.16}$$

$$\delta = \arctan\left(\frac{\dot{q}\sin t + q\cos t}{\dot{q}\cos t - q\sin t}\right) \tag{4.17}$$

The net forces acting due to the springs which are the internal forces are already know in the form of F_q (Equations 3.29 to 3.32). The normal force F_n is the cosine component of the internal force F_q with the angle (90-δ) as depicted in Figure 4.6. Hence the frictional force as depicted in the Coulomb's model (Van Geffen (2009)) can be written as:

$$F_f = \mu F_n \mathrm{sign}(\dot{q}) \tag{4.18}$$

$$F_f = \mu(F_q\cos(90-\delta))\mathrm{sign}(\dot{q}) \tag{4.19}$$

Where F_f = Frictional force, μ = Co-efficient of friction (0.14), F_n = Normal Force, δ = Angle found from the slope of the tangent to the curve given by the sine component of the net force.

4.3.1 Loss of Power

Consequently the power loss at each DOF can also be calculated. This is with reference to the power loss and efficiency calculations mentioned in Section 3.4.3. The theoretical power loss at each of the DOFs can be computed as:

$$P_{\text{losses}} = F_f \cdot \dot{q} \tag{4.20}$$

Let $P_{\text{input}} = P_q$ be the input power on the DOF without the losses. Due to losses, the input power should change to $P_{\text{input}} = P_q + P_{\text{losses}}$.

In order to find the efficiency of the DOFs individually, as stated in equation 3.37, the output power from the DOF is considered P_q, then we can formulate it as:

$$\eta = \frac{\text{Power Output}}{\text{Power Input}} \times 100 \tag{4.21}$$

$$\eta = \frac{P_q}{P_q + P_{\text{losses}}} \times 100 \tag{4.22}$$

A plot of the aforementioned in comparison to the values of P_q has been presented in Figure 4.7. We can see here the power input, power loss and the power input with the addition of the losses. In comparison to the results in Chapter 3 (Figure 3.11), the plots are similar in nature and have an identical magnitude. The nature of the losses of this theoretical analysis seem to follow a similar pattern to that of the black-box model.

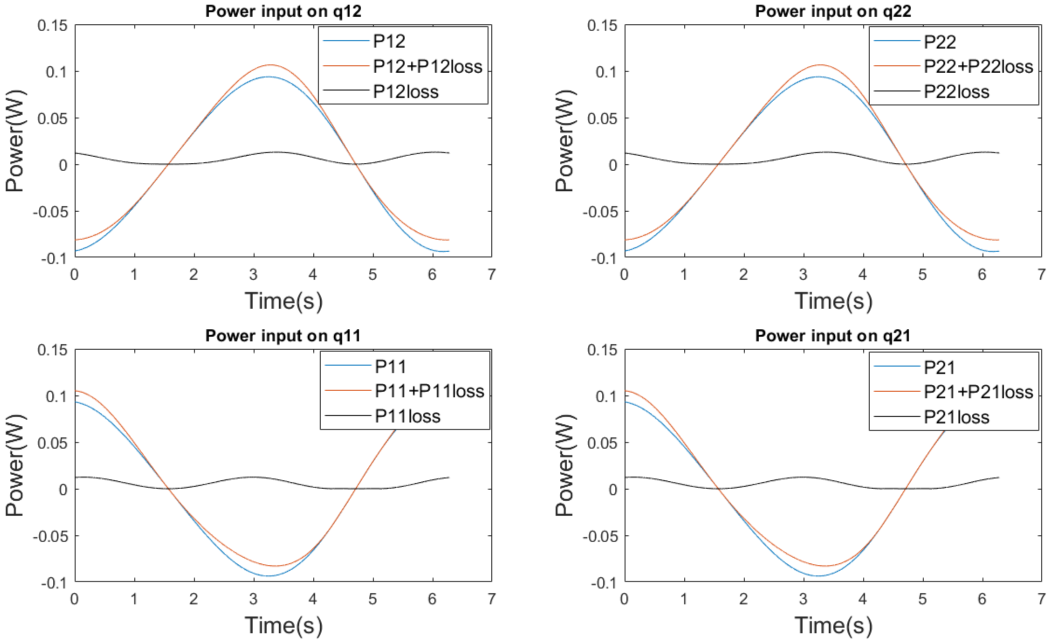

Figure 4.7: Comparison between input power (Pij), input power with losses(Pij+Pijloss) and the power loss(Pijloss), where i,j ∈ {1,2}.

4.3.2 Efficiency of the new system

The efficiency plots of the DOFs for the new proposed model is shown in Figure 4.8. The mean efficiency of the DOFs q_{12} and q_{22} was calculated to be 93.03% and for the DOFs q_{11} and q_{21} was found to be 93.39%. In comparison to the results obtained at the end of chapter 3, the mean efficiency of the theoretical model is higher in comparison to the black box model. The efficiency plots are slightly different as the peaks in the theoretical model. Like the plots in Figure 3.12, the peaks here are not as sharp. Also for q_{11} and q_{21}, there is a cluster of three peaks. These behaviours are likely due to the geometry of the spirals along which the DOFs are guided.

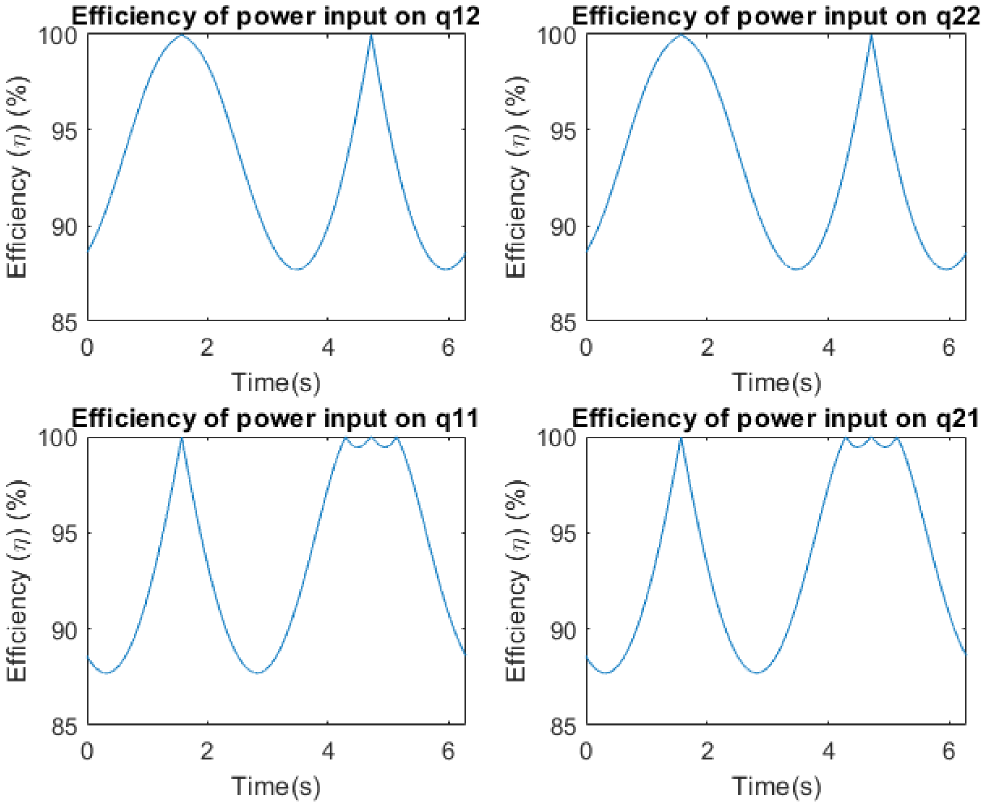

Figure 4.8: Efficiency of power input on the DOFs over time.

4.3.3 Use of Compensation Springs

With the inclusion of compensation springs these losses can be reduced, thereby allowing the system to achieve maximum efficiency. This means that the springs can overcome the loss of power in the DOFs i.e. $F_{\text{losses}} + F_{\text{comp}} = 0$. This is illustrated in Figure 4.9. This results in zero power loss in the DOFs. It indicates that the resultant power input at the control port is zero. The idea of using compensation springs comes from static balancing mechanisms which are mentioned at the end of Chapter 2, especially the spring to spring balancer mentioned in Figure 2.4. The efficiency plot of the effect of the spring compensation can be seen in Figure 4.10.

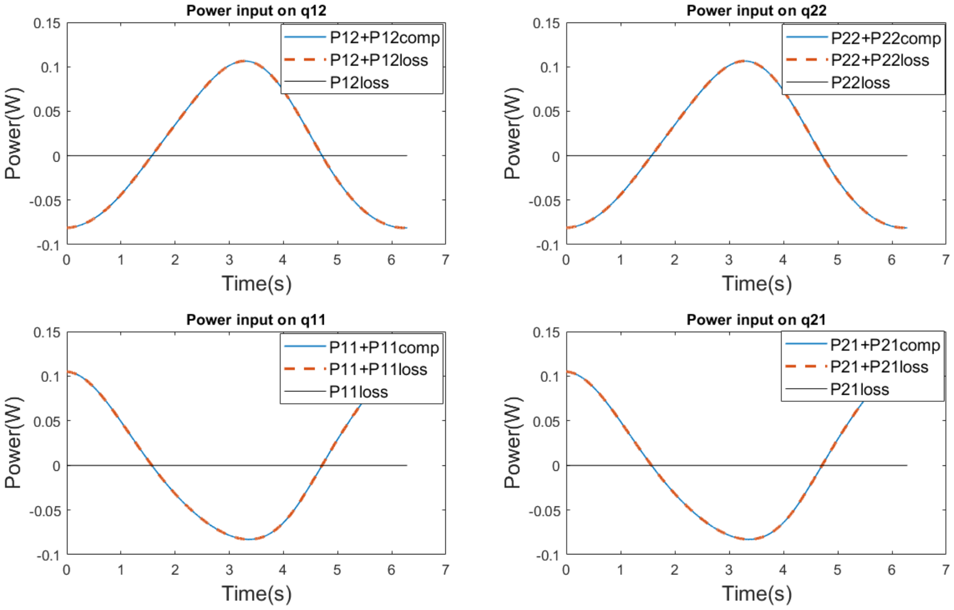

Figure 4.9: Power on the DOFs using compensation springs.

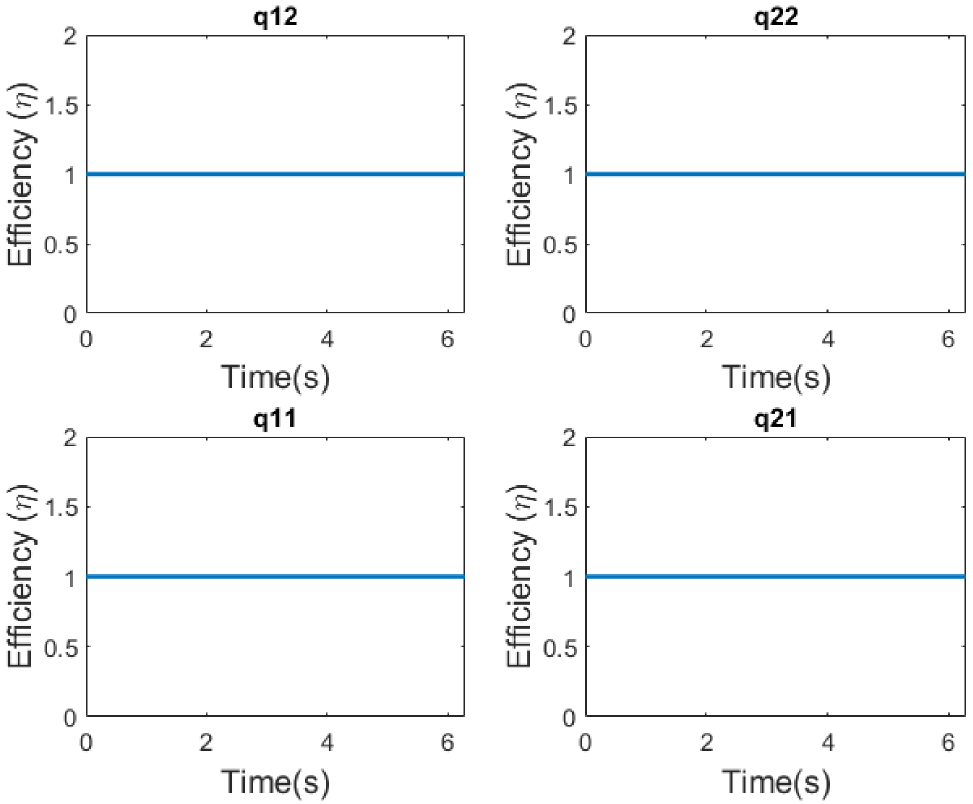

Figure 4.10: Efficiency of power input on DOFs using compensation springs.

4.4 Inference

The synthesis of the DOFs with the help of different mechanical components can help realize the motion trajectories. Also it can achieve the objectives of reducing the DOFs by coupling them and compensate the reaction forces. The motion trajectories can be manifested with the help of the motion spirals. Making a hollow cut out of the entire profile on a wheel/gear would be practically impossible. Therefore a part of the spiral can be carved out in the form of a groove with a certain thickness. This can be done considering the lines shown in the plots as the center, that would deem suitable to attain the goal. An example of a CAD design of a wheel containing a spiral is shown in Figure 4.11. The choice behind having the motion spirals from angles $-\pi/2$ to $\pi/2$ is to have a rotation of 180° both in the clockwise and anticlockwise direction respectively. Therefore it would account for a full rotation. A non-hollow groove maybe chosen but that would lead to increased frictional losses.

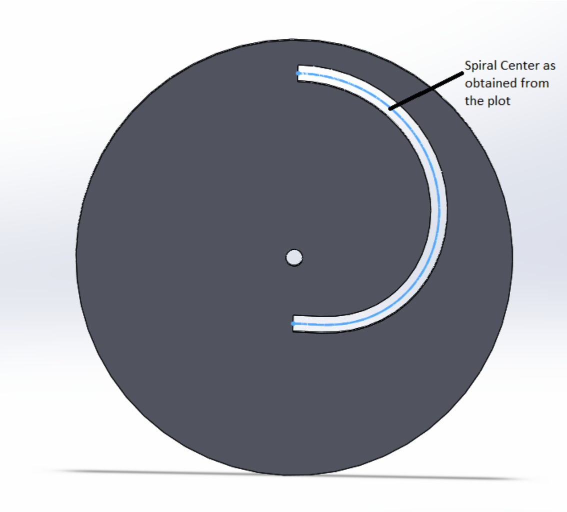

Figure 4.11: CAD design of a hollow spiral groove carved on a wheel (diameter =13 cm).

The same applies to the force spirals. Also it is convenient to have two force spirals on one wheel/gear to compensate the forces on either of motion spirals on the left and right side. This would reduce the number of components and the overall size of the system.

Friction always plays an important role in any mechanical system. For the current system the friction model has been calculated and the estimated range for the compensation forces is shown. Nonetheless, when this developed into hardware, the losses due to friction may not be uniform at all instances as it will also depend on the physical properties such as the amount of contact between the two surfaces, smoothness/roughness of the material use, etc. So there is chance that it may deviate at certain instances in comparison to the plots obtained currently. There can be probable peaks and troughs in the compensation force plots which will depict the non-uniform behaviour of the system due to fricition when the system is implemented in real life. The loss of power can hence be calculated to check the efficiency of the system. The role of the compensation springs has been illustrated as to how to make up for this lost power.

5 Conclusion and Future Recommendations

This chapter presents the conclusion of the research, discusses limitations of the new proposed design and the recommendations that can possibly be implemented in the future.

5.1 Conclusion

Variable stiffness mechanisms are employed in the field of robotics for tasks mainly dealing with replicating human movement. Traditional robots are unable to achieve this behaviour due to their fixed compliance properties and their stiff nature. In this report we discuss such a mechanism that utilises variable stiffness, i.e a cable driven Variable Stiffness Actuator (VSA) and aim to satisfy the design goals.

There already exists a system with a certain stiffness change profile which has four actuated DOFs. But the presence of multiple DOFs deemed it unfeasible to be used as it is for assistive applications due to design complications. The first design goal was to reduce these DOFs and device a mechanism with reduced actuated DOF. The results of the motion trajectories obtained from the current system suggested that system can be coupled to achieve the desired stiffness change without changing the equilibrium position. This can be done mechanically using a timing belt to connect the wheels/gears with the cam profiles of the motion trajectories. The system was therefore designed keeping the output angle ($\theta = 0$) and change in the output torque ($\dot{\tau} = 0$). The choice of keeping the change in torque constant was done keeping in mind the use of the VSA in an arm support. If we consider the elbow at an angle of 90°, then the force due to gravity of an object placed on the hand or palm is balanced out by the mechanism. Keeping the change in torque constant would suggest that the force remains unchanged when the stiffness changes, thereby suggesting there is no acceleration. Meaning that there would be no oscillations. Usually the damping of oscillations is essentially done with the help of controls. But since this project doesn't deal with it, making this choice simplifies the objective.

The second goal was to make the system more efficient. Initially it was thought that removal of the four servomotors (that drove the DOFs) would lead to the internal forces to act on the DOFs. This would require some energy injection at the input if not compensated. So static balancing techniques such as compensation springs would be required. However, this was not the case. This is by construction and the choice of keeping θ=0 as mentioned in the above paragraph. Hence, the compensation springs are not required to balance the internal forces. The energy content of the coupled system was calculated to be constant which meant that the control power was zero. What required attention was the loss due to friction that were a result of the interaction between the various parts of the system.

The results of section 3.4.3 indicated that the computed losses could be mitigated with the help of compensation springs. An estimate of the loss was computed using a black-box model in Chapter 3 to which the theoretical model of the new system was compared. Comparing the power plots of the two models it could be observed that the results of the theoretical model were close to the black-box model. However, it differed in certain instances, the average deviation of the losses in the black-box model being 10^{-3} W higher than the theoretical model.

There are discrepancies noticed while comparing the efficiency plots 3.12 and 4.8 in Chapter 3 and 4 respectively which meant the theoretical results were not the exact same as the black-box model. This is due to the fact that the geometry of the spirals designed in Chapter 4 and their contact with the DOFs (pins) were not accounted for in the black-box model, which was estimated to be a regular circular motion. This is why the mean efficiency of the theoretical model was higher than the black-box model.

The results obtained for the inclusion of the compensation springs conclude that the losses due to friction can be mitigated. Since the condition that was chosen for $P_{\text{control}} = 0$ was $F_{\text{comp}} + F_{\text{losses}} = 0$, the springs were able to mitigate the losses completely and this resulted in establishment of an ideal system. The DOFs are considered as mass-less or point masses, so there is no loss due to damping ideally. But in practicality, there will be damping losses resulting in some non-zero power input. Also the arrangement of the practical setup may change the frictional forces. There will also be some friction losses due to the pin sliding against the straight grooves. In those cases there may be instances of deviation from the theoretical model, but by and large the springs should be able to compensate for the unexpected increase in losses if they are within a certain range. In the real model, the input power through the control port must be observed in order to estimate how close it is to the ideal model. To make a more realistic estimate of the system, the mass of the pins must be know to calculate the damping loss. Also the material of the straight groove should be considered which is explained in detail in the next subsection.

5.1.1 Discussion

The use of a single actuated DOF input that causes the equilibrium position to remain unchanged can be seen as a design limitation. This was done for simplification purposes and can be solved with having two actuated DOFs for either tendons. This could further help study how the stiffness change will occur at a different equilibrium position. Or whether the same stiffness change profile can be chosen for a different equilibrium position i.e. $\theta \neq 0$, corresponding to a particular energy content. Hypothetically, the system should at a changed equilibrium configuration be able to achieve a desired stiffness profile, but the motion trajectories would completely change. When changed to a different stiffness, the motion trajectories would change once again. Combination of multiple trajectories for different configurations may lead to difficulty in realising the system on a single disc.

The loss that was not accounted for in the system was the friction between the pin and the straight (horizontal) grooves. Even though the contact between the two will be lesser than that in comparison to the one between the pin and spirals, there will be some effect on the losses. In order to calculate this loss, the mass of the pin must be known along with the material of the straight (horizontal) groove and the area of contact between the two surfaces. These losses must be added to the already existing friction loss in the system to get a better estimate of the losses and efficiency. Also this would test the effectiveness of the springs to mitigate the losses. This can only be estimated if all the parameters of the hardware are known and would result in a much accurate theoretical model for the losses.

In order to make a theoretical analysis of these losses, let us consider the mass of the pin of mass m. Let g the acceleration due to gravity. The normal force (N) is given by:

$$N = mg \tag{5.1}$$

Let μ_h be the friction constant between the pin and the straight groove. The friction force (F_h) can then be computed by:

$$F_h = \mu_h N \text{sign}(v) \tag{5.2}$$

where v is the sliding velocity of the pin. In our friction model we consider $F_h << F_f$ (where F_f is the frictional force between the pin and the spiral wall, refer to Equation 4.18) and hence it is neglected for the reasons mentioned above. But to obtain a more accurate model for the losses in the system the total loss should be written as $F_{\text{losses}} = F_f + F_h +$ Damping losses from the springs. This can done only when all the parameters stated above are known when the model is physically built. The damping loss factor can then also be computed to determine the actual losses in the system for a non-ideal case. This is why the theoretical model was designed only using F_f as a loss.

5.2 Future Recommendations

The first step would be to build the new system as proposed with the motion and force wheels/gears, timing belt, pins and springs. Additional equipment such as bearings maybe used to constrain the motions and reduce the internal frictional losses. After the construction is done, experiments for measurement of input force/torque and power must be done with and without the springs. An estimated outcome from the experiments should be the use of the springs to reduce the losses. It must be inspected how well and to what extent they mitigate these losses. The power input must be closer to zero for the case with the springs in comparison to the experiment without them. The force and torque can be measured by using a F/T sensor through which can be mounted on top of the input. It would rotate as an when the input hand crank is rotated. The consequent power input can the be calculated.

The new system is deemed to be larger in size than the already existing one. This is because the system is a proof of principle for achieving the aforementioned goals of the project. If the prototype is in sync with the results of the theoretical analysis, then further research needs to be done to downsize the system. This would require kinematic calculations in 3D as opposed to the 2D calculations done for this research. The implementation of such a system would have the force spiral wheel/gear elevated as compared to the motion spiral wheels/gears to save space. In that way the system can be made more compact.

A Appendix 1: Uncompensated Internal Forces

In a case where the internal forces in the system are not compensated due to construction of the VSA. Or if the system is asymmetric which results in the internal forces to be present in the system, the compensation force from the springs will always range between a maximum and minimum value. Any added force beyond its maximum limit cannot be compensated for by it. This can be computed as follows:

From the friction calculations in Chapter 3 Section 4.3 calculations the values for the factors A and B could be determined by plugging in the values of the corresponding data.

The factors in general can be calculated as a ratio of the difference between the force applied by the cable on the DOFs (F_q) and the frictional force (F_f) to the force applied by the cable on the DOFs (F_q). A general equation for a ratio factor RF can be expressed as:

$$RF = \frac{F_q - F_f}{F_q} \tag{A.1}$$

Consequently the values for A and B can be found by finding out the minimum and maximum values within the range respectively i.e. A=min(RF) and B=max(RF).

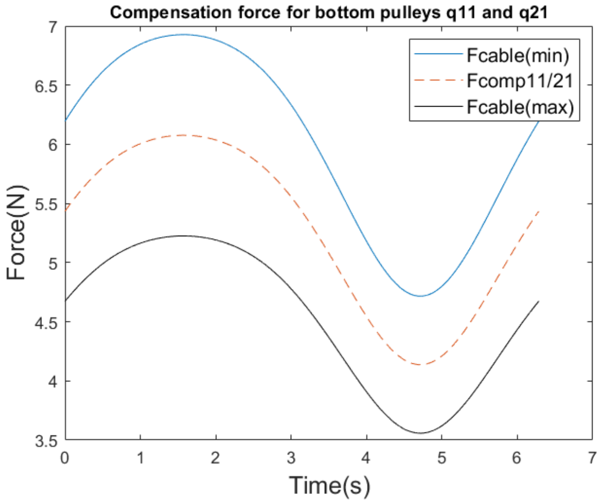

Figure A.1: Range of the compensation force due to friction for q_{11} and q_{21}.

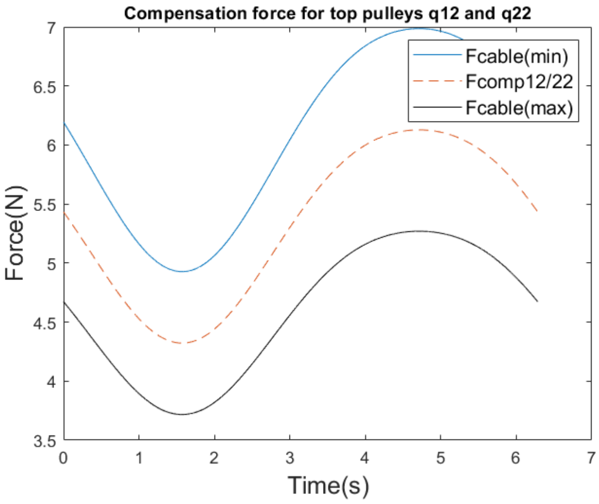

Figure A.2: Range of the compensation force due to friction for q_{12} and q_{22}.

It was found for a friction coefficient (μ) = 0.14 between the pin (made of steel) and the spiral (made of POM), the spring compensation force for DOFs q_{11} and q_{21} was between (Figure A.1):

$$0.86 \cdot F_{\text{cable}} \leq F_{\text{comp}} \leq 1.14 \cdot F_{\text{cable}} \tag{A.2}$$

And for the DOFs q_{12} and q_{22}, the values for the spring force lie between (Figure A.2):

$$0.84 \cdot F_{\text{cable}} \leq F_{\text{comp}} \leq 1.16 \cdot F_{\text{cable}} \tag{A.3}$$

From the above calculations it can be inferred that the compensation force will never be equal to F_q as there will be losses incurred due to friction.

B Appendix 2: Dimensions of the Reduced DOF Model

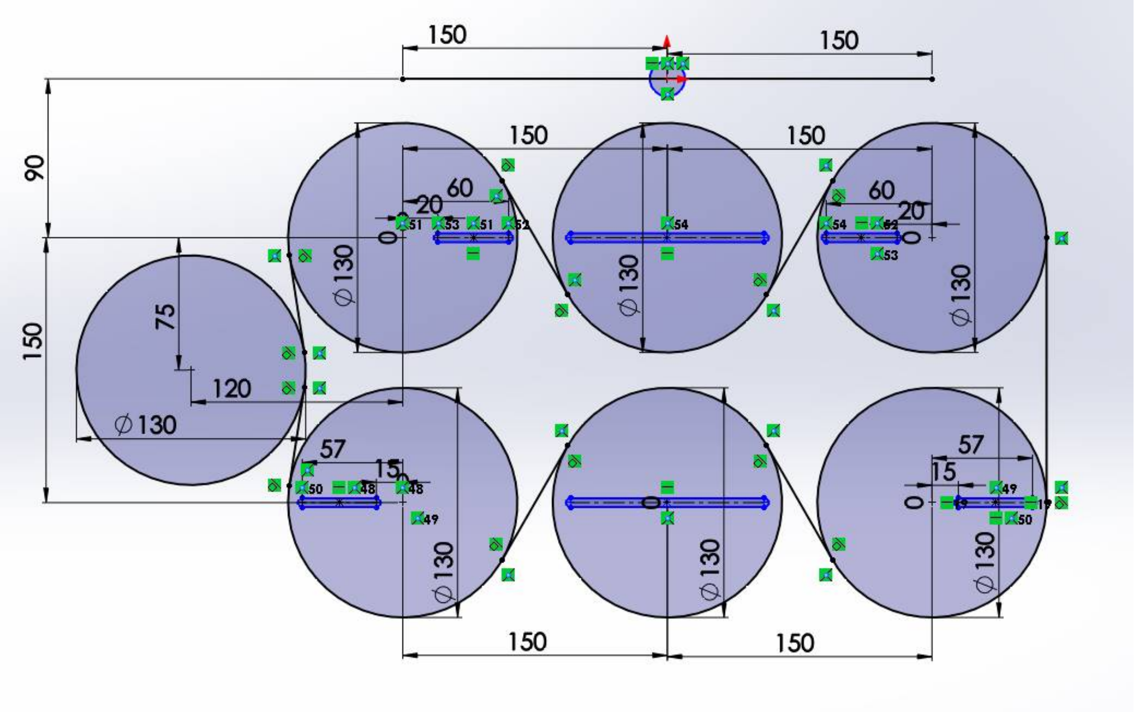

Figure B.1: Dimensions of the reduced DOF Model

Dimensions of the existing model in Groothuis et al. (2020) are as follows:
$l_\theta = d_\theta = 90$ mm (total length of the output bar = 180 mm)
$a_1 = a_2 = 90$ mm
$b_1 = b_2 = 100$ mm
$c_1 = c_2 = 80$ mm
$d_1 = d_2 = 140$ mm

Dimensions of the new proposed model:
$l_\theta = d_\theta = 150$ mm (total length of the output bar = 300 mm)
$a_1 = a_2 = 90$ mm
$b_1 = b_2 = 150$ mm
$c_1 = c_2 = 90$ mm
$d_1 = d_2 = 140$ mm

C Appendix 3: MATLAB Script

```
%% qdot
clear all;
clc;
load q11.mat
load q12.mat
load q21.mat

x=[]; %total time period (s)
k=0;
for t=0:0.001:2*pi %range for time period
    k=k+1;
    x(k)=t;
end

%% q11dot

%%Kdes=0.5cos(t)
%coefficients for the Fourier series for q11 and q21
a0=0.0387178;
a2=0.00131169;
a4=-0.0000305498;
b1=0.0175825;
b3=-0.00015739;
b5=5.28572*10^(-6);


q11=a0 + a2* cos(2*x) +a4* cos(4*x) + b1*sin(x) + b3*sin(3*x) + b5*sin(5*x); %Motion equation for q11
q11dot=5*b5*cos(5*x)-4*a4*sin(4*x)+3*b3*cos(3*x)-2*a2*sin(2*x)+b1*cos(x);%Velocity equation for q11
figure;
plot(x,q11); %Displacement plot
xlabel('Time(s)');
ylabel('Displacement(m)');
title('Motion of pulley (q11)');
figure;
plot(x,q11dot);%Velocity plot
xlabel('Time(s)');
ylabel('Velocity(m/s)');
title('Velocity of pulley (q11)');
 q11per=abs(Val1-q11.'); %Displacement difference
     per11=[6284,1];
    for i=1:6284
    per11(i)=(q11per(i)/Val1(i))*100; %Displacement difference (in %)
    end

%Kdes=0.5cos(t)
```

```
%coefficients of the Fourier series for q12 and q22
a0x=0.0397704;
a2x=0.00023253;
a4x=-3.0255*10^(-6);
b1x=-0.0172983;
b3x=0.0000551443;
b5x=-4.64409*10^(-7);

q12= a0x + a2x*cos(2*x)+ a4x*cos(4*x) +b1x*sin(x) + b3x*sin(3*x)+ b5x*sin(5*x);%Motion equation for q12
q12dot=5*b5x*cos(5*x)-4*a4x*sin(4*x)+3*b3x*cos(3*x)-2*a2x*sin(2*x)+ b1x*cos(x);%Velocity equation for q12
figure;
plot(x,q12);%Displacement plot
xlabel('Time(s)');
ylabel('Displacement(m)');
title('Motion of pulley (q12)');
figure;
plot(x,q12dot);%Velocity plot
xlabel('Time(s)');
ylabel('Velocity(m/s)');
title('Velocity of pulley (q12)');
 q12per=abs(Val2-q12.');%Displacement difference
      per12=[6284,1];
     for i=1:6284
     per12(i)=(q12per(i)/Val2(i))*100;%Displacement difference(in %)
     end
q22=q12; %Equality between q22 and q12
q21=q11; %Equality between q21 and q11
q21dot=q11dot; %Equality between q21dot and q11dot
q22dot=q12dot; %Equality between q22dot and q12dot
%% Force Profile
%Dimensions of the tendons of the current system
a1=0.09;
a2=0.09;
b1=0.15;
b2=0.15;
c1=0.09;
c2=0.09;
d1=0.14;
d2=0.14;
ltheta=0.15; %total length of the output bar
dtheta=0.15; %total length between the attachment points on the output bar
theta=0;
Lbar=0.445; %pretension
k=100;
L1=d1+sqrt(c1^2+q11.^2)+sqrt(b1^2+(q11+q12).^2)+sqrt((-ltheta+ dtheta*cosd(theta)+q12).^2+(a1-ltheta*sind(theta)).^2); %Left tendon dimension
```

```
L2=d2+sqrt(c2^2+q21.^2)+sqrt(b2^2+(q21+q22).^2)+sqrt((-ltheta+dtheta*cosd(theta)+q22).^2+(a2+ltheta*sind(theta)).^2); %Right tendn dimension
s1=L1-Lbar; %change in cable length for L1
s2=L2-Lbar; %change in cable length for L2
F1=k*s1; %Force on left tendon
F2=k*s2; %Force on right tendon
figure;
plot(x,F1); %Force on left tendon plot
xlabel('Time(s)');
ylabel('Force(N)');
title('Force on left side of the system ');
figure;
plot(x,F2); %Force on right tendon plot
xlabel('Time(s)');
ylabel('Force(N)');
title('Force on right side of the system ');
alpha=[1,6284];
beta=[1,6284];
gamma=[1,6284];
delta=[1,6284];
for i=1:6284
alpha(i)=atand(a1/q12(i)); %angle extended between a1 and q12
beta(i)=atand(b1/(q12(i)+q11(i)));  %angle extended between b1 and q12 & q11
gamma(i)=atand(b1/(q11(i)+q12(i))); %angle extended between c1 and q12 & q11
delta(i)=atand(c1/q11(i)); %angle extended between c1 and q11
end
%Internal forces
 Fnetq12=F1.*cosd(alpha)+F1.*cosd(beta); %Force on q12
 Fnetq11=F1.*cosd(gamma)+F1.*cosd(delta); %Force on q11
 Fnetq21=F2.*cosd(gamma)+F2.*cosd(delta); %Force on q21
 Fnetq22=F2.*cosd(alpha)+F2.*cosd(beta); %Force on q22

figure;
plot(x,Fnetq12); %Forces on q12 and q22
xlabel('Time(s)');
ylabel('Force(N)');
title('Force exerted by the cables on the pulleys');
hold on;
plot(x,Fnetq11); %Forces on q11 and q21
xlabel('Time(s)');
ylabel('Force(N)');
hold on;
legend('Fnetq12 & Fnetq22','Fnetq11 & Fnetq21');
Fnet=Fnetq12+Fnetq11; %Total net force
%% Force vs Displacement
figure;
lin12= 52.24*q12 + 3.253; %Linear fit for q12 and q22
lin11= 54.5*q11 + 3.164; %Linear fit for q11 and q21
```

```
% Plotting all forces with respect to their absolute distances
subplot(2,2,1)
plot(q12,Fnetq12,'red');
hold on
plot(q12,lin12,'black');
xlabel('q12 (m)');
ylabel('Fnetq12 (N)');
title('Fnetq12 vs q12');
legend ('Fnetq12 vs q12','Linear Fit');
subplot(2,2,2)
plot(q22,Fnetq22,'red');
hold on
plot(q12,lin12,'black');
xlabel('q22 (m)');
ylabel('Fnetq22 (N)');
title('Fnetq22 vs q22');
legend ('Fnetq22 vs q22','Linear Fit');
subplot(2,2,3)
plot(q11,Fnetq11,'red');
hold on
plot(q11,lin11,'black');
xlabel('q11 (m)');
ylabel('Fnetq11 (N)');
title('Fnetq11 vs q11');
legend ('Fnetq11 vs q11','Linear Fit');
subplot(2,2,4)
plot(q21,Fnetq21,'red');
hold on
plot(q11,lin11,'black');
xlabel('q21 (m)');
ylabel('Fnetq21 (N)');
title('Fnetq21 vs q21');
legend ('Fnetq21 vs q21','Linear Fit');
%% Spiral
% Polar coordinates of the displacements of the various DOFs
x11=q11.*cos(x);
y11=q11.*sin(x);
x12=q12.*cos(x);
y12=q12.*sin(x);
x21=q21.*cos(x);
y21=q21.*sin(x);
x22=q22.*cos(x);
y22=q22.*sin(x);

% Polar plots of the displacements of the various DOFs that can be
    transformed into a spiral
figure;
subplot(2,2,1)
plot(x12,y12);
xlabel('q12cos(x) [m]');
ylabel('q12sin(x) [m]');
```

```
title('Motion Spiral q12');

subplot(2,2,2)
plot(x22,y22);
xlabel('q22cos(x) [m]');
ylabel('q22sin(x) [m]');
title('Motion Spiral q22');

subplot(2,2,3)
plot(x11,y11);
xlabel('q11cos(x) [m]');
ylabel('q11sin(x) [m]');
title('Motion Spiral q11');

subplot(2,2,4)
plot(x21,y21);
xlabel('q21cos(x) [m]');
ylabel('q21sin(x) [m]');
title('Motion Spiral q21');
%% Force Spiral

% coordinates of the distance traversed by the compensation springs
s_theta12_k2=q12+Fnetq12/140;
s_theta21_k2=q21+Fnetq21/140;
s_theta11_k2=q21+Fnetq21/140;
s_theta22_k2=q12+Fnetq12/140;

% adding a shift in coordinates of the distance traversed
s_theta12_shift=s_theta12_k2-(min(s_theta12_k2)-0.01);
s_theta21_shift=s_theta21_k2-(min(s_theta21_k2)-0.01);
s_theta11_shift=s_theta11_k2-(min(s_theta11_k2)-0.01);
s_theta22_shift=s_theta22_k2-(min(s_theta22_k2)-0.01);

% Polar coordinates of the distances traversed by the compensation
    springs for
% q12
ssxk12=s_theta12_shift.*cos(x);
ssyk12=s_theta12_shift.*sin(x);

%q21
ssxk21=s_theta21_shift.*cos(x);
ssyk21=s_theta21_shift.*sin(x);

%q11
ssxk11=s_theta11_shift.*cos(x);
ssyk11=s_theta11_shift.*sin(x);

%q22
ssxk22=s_theta22_shift.*cos(x);
ssyk22=s_theta22_shift.*sin(x);

```

```
% Polar coordinates of the distances traversed by the compensation springs
subplot(2,2,1)
plot(ssxk12,ssyk12);
title('Force spiral for q12');
xlabel('scos(x) [m]');
ylabel('ssin(x) [m]');

subplot(2,2,2)
plot(ssxk22,ssyk22);
title('Force spiral for q22');
xlabel('scos(x) [m]');
ylabel('ssin(x) [m]');

subplot(2,2,3)
plot(ssxk11,ssyk11);
title('Force spiral for q11');
xlabel('scos(x) [m]');
ylabel('ssin(x) [m]');

subplot(2,2,4)
plot(ssxk21,ssyk21);
title('Force spiral for q21');
xlabel('scos(x) [m]');
ylabel('ssin(x) [m]');

%Curve fit for the cartesian coordinates of the force spirals for verification
sshift12=0.03479+1.588*10^(-6)*cos(x)+0.000977*cos(2*x)+1.933*10^(-8)*cos(3*x)-0.02374*sin(x)-5.671*10^(-7)*sin(2*x)+5.804*10^(-5)*sin(3*x);
sshift21=0.0372-3.992*10^(-7)*cos(x)+0.002479*cos(2*x)+1.719*10^(-8)*cos(3*x)+0.02438*sin(x)+2.257*10^(-7)*sin(2*x)-0.0002841*sin(3*x);

%% Friction
%q11 and q21
dy21=(q21dot.*sin(x)+q21.*cos(x)); %dy for q21 and q11
dx21=(q21dot.*cos(x)-q21.*sin(x)); %dx for q21 and q11
tangent21=[1,6284];
si21=[1,6284];
for i=1:6284
tangent21(i)= dy21(i)/dx21(i);%slope of the tangent
si21(i)=atand(tangent21(i));%angle of the slope of the tangent
end
Fcomp21=0.14.*Fnetq21.*cosd(90-si21).*sign(q21dot);%Frictional force on q21 and q11
Fcomp21copy=0.14.*Fnetq21.*cosd(90-si21);
fact21=[1,6284];
for i=1:6284
```

```
fact21(i)=(Fnetq21(i)-Fcomp21(i))/Fnetq21(i);%Ratio factor for q21 and q11
end
maxlimit21=max(fact21); %maxlimit B for q21 and q11
minlimit21=min(fact21); %minlimit A for q21 and q11
figure;
plot(x,maxlimit21*Fnetq21); %plot of maxlimit
hold on;
plot(x,Fnetq21,'--'); %plot of optimum force
hold on;
plot(x,minlimit21*Fnetq21,'black');%plot of minlimit
xlabel('Time(s)','FontSize',15);
ylabel('Force(N)','FontSize',15);
legend('Fcable(min)','Fcomp11/21','Fcable(max)','FontSize',12);
title('Compensation force for bottom pulleys q11 and q21');

% q12 and q22
dy12=(q12dot.*sin(x)+q12.*cos(x)); %dy for q12 and q22
dx12=(q12dot.*cos(x)-q12.*sin(x)); %dx for q12 and q22
tangent12=[1,6284];
si12=[1,6284];
for i=1:6284
tangent12(i)= dy12(i)/dx12(i);%slope of the tangent
si12(i)=atand(tangent12(i));%angle of the slope of the tangent
end
Fcomp12=0.14.*Fnetq12.*cosd(90-si12).*sign(q12dot);%Frictional force on q12 and q22
Fcomp12copy=0.14.*Fnetq12.*cosd(90-si12);
fact12=[1,6284];
for i=1:6284
fact12(i)=(Fnetq12(i)-Fcomp12(i))/Fnetq12(i);%Ratio factor for q12 and q22
end
maxlimit12=max(fact12); %maxlimit A for q12 and q22
minlimit12=min(fact12); %minlimit A for q12 and q22
figure;
plot(x,maxlimit12*Fnetq12); %plot of maxlimit
hold on;
plot(x,Fnetq12,'--'); %plot of optimum force
hold on;
plot(x,minlimit12*Fnetq12,'black'); %plot of minlimit
xlabel('Time(s)','FontSize',15);
ylabel('Force(N)','FontSize',15);
legend('Fcable(min)','Fcomp12/22','Fcable(max)','FontSize',12);
title('Compensation force for top pulleys q12 and q22');

%% Power
% Plotting the power acting on the individual DOFs
figure;
p11=Fnetq11.*q11dot; %power on q11
subplot(2,2,3)
```

```
plot(x,p11);
xlabel('Time(s)');
ylabel('Power(W)');
title('Power input on q11');

p12=Fnetq12.*q12dot; %power on q12
subplot(2,2,1)
plot(x,p12);
xlabel('Time(s)');
ylabel('Power(W)');
title('Power input on q12');

p21=Fnetq21.*q11dot; %power on q21
subplot(2,2,4)
plot(x,p21);
xlabel('Time(s)');
ylabel('Power(W)');
title('Power input on q21');

p22=Fnetq22.*q12dot; %power on q22
subplot(2,2,2)
plot(x,p22);
xlabel('Time(s)');
ylabel('Power(W)');
title('Power input on q22');

p=[];
for i=1:6284
    p(i)=p11(i)+p12(i)+p21(i)+p22(i); %total power
end
figure;
plot(x,p,'LineWidth',2); %plot of total power vs time
xlabel('Time(s)');
ylabel('Power(W)');
ylim([-0.1 0.1])
title('Total input power in the system');

E=0.5*k*(s1.^2+s2.^2); %Energy content of the system
figure;
plot(x,E,'Linewidth',2) %plot of the energy content over time
xlabel('Time(s)');
ylabel('Energy(J)');
ylim([0.384 0.3842])
title('Total Energy content of the system');

q11temp1=[];
q11temp2=[];
q21temp1=[];
q21temp2=[];
q12temp1=[];
q12temp2=[];
```

```
q22temp1=[];
q22temp2=[];
v1temp1=[];
v1temp2=[];
v1temp3=[];
v1=[];
v2=[];
P1=[];
for i=1:6284
    q11temp1(i)=q11(i)/sqrt(q11(i)^2+c1^2);
    q11temp2(i)=(q11(i)+q12(i))/sqrt(b1^2+(q11(i)+q12(i))^2);
    Fq11(i)=F1(i)*(q11temp1(i)+q11temp2(i)); %Force on q11

    q21temp1(i)=q21(i)/sqrt(q21(i)^2+c2^2);
    q21temp2(i)=(q21(i)+q22(i))/sqrt(b2^2+(q21(i)+q22(i))^2);
    Fq21(i)=F2(i)*(q21temp1(i)+q21temp2(i)); %Force on q21

    q12temp1(i)=(q11(i)+q12(i))/sqrt(b1^2+(q11(i)+q12(i))^2);
    q12temp2(i)=(dtheta*cosd(theta)-ltheta+q12(i))/sqrt((a1-ltheta*sind(theta))^2+(dtheta*cosd(theta)-ltheta+q12(i))^2);
    Fq12(i)=F1(i)*(q12temp1(i)+q12temp2(i)); %Force on q12

    q22temp1(i)=(q21(i)+q22(i))/sqrt(b2^2+(q21(i)+q22(i))^2);
    q22temp2(i)=(dtheta*cosd(theta)-ltheta+q22(i))/sqrt((a1-ltheta*sind(theta))^2+(dtheta*cosd(theta)-ltheta+q22(i))^2);
    Fq22(i)=F2(i)*(q22temp1(i)+q22temp2(i)); %Force on q22

    v1temp1(i)=(q11(i)*q11dot(i))/sqrt(c1^2+q11(i)^2);
    v1temp2(i)=((q11(i)+q12(i))*(q11dot(i)+q12dot(i)))/sqrt(b1^2+(q11(i)+q12(i))^2);
    v1temp3(i)=((-ltheta+dtheta*cosd(theta)+q12(i))*q12dot(i))/(sqrt((a1-ltheta*sind(theta))^2+(-ltheta+dtheta*cosd(theta)+q12(i))^2));
    v2(i)=((q21(i)*q21dot(i))/sqrt(c2^2+q21(i)^2)+((q21(i)+q22(i))*(q21dot(i)+q22dot(i)))/sqrt(b2^2+(q21(i)+q22(i))^2)+((-ltheta+dtheta*cosd(theta)+q22(i))*q22dot(i))/(sqrt((a2+ltheta*sind(theta))^2+(-ltheta+dtheta*cosd(theta)+q22(i))^2)));
    P1(i)=F1(i)*(v1temp1(i)+v1temp2(i)+v1temp3(i)); % total power in left tendon
    P2(i)=F2(i)*v2(i); %total power in right tendon
end
% Work done on individual DOFs
Wq11=trapz(q11,Fq11);
Wq21=trapz(q21,Fq21);
Wq12=trapz(q12,Fq12);
Wq22=trapz(q22,Fq22);
Wtotal=Wq11+Wq12+Wq21+Wq22;

figure;
plot(x,P1+P2,'Linewidth',2); %plot of total power in the system
```

```
xlabel('Time(s)');
ylabel('Power(W)');
ylim([-0.1 0.1])
title('Total power present in the system');


% Kr=tau_theta./;
% figure;
% plot(x,Kr);
% xlabel('Time(s)');
% ylabel('Stiffness range (Nm/rad)');

Px=Fq11.*q11dot+Fq12.*q12dot; %Power on left tendon
Py=Fq21.*q21dot+Fq22.*q22dot; %Power on right tendon
%% Power loss and efficiency
% Power loss on various DOFs and their plots vs time
Ploss11=Fcomp21.*q11dot; %power loss on q11
Ploss21=Fcomp21.*q21dot; %power loss on q21
Ploss12=Fcomp12.*q12dot; %power loss on q12
Ploss22=Fcomp12.*q22dot; %power loss on q22

p11min=minlimit21.*p11; %min power loss on q11
p11max=maxlimit21.*p11; %max power loss on q11
figure;
subplot(2,2,3)
plot(x,p11,'--');
hold on
plot(x,p11min);
hold on
plot(x,p11max);
xlabel('Time(s)');
ylabel('Power(W)');
title('Power input with springs on q11');
legend('Optimum Power','Pmin','Pmax');

p12min=minlimit12.*p12;%min power loss on q12
p12max=maxlimit12.*p12;%max power loss on q12
subplot(2,2,1)
plot(x,p12,'--');
hold on
plot(x,p12min);
hold on
plot(x,p12max);
xlabel('Time(s)');
ylabel('Power(W)');
title('Power input with springs on q12');
legend('Optimum Power','Pmin','Pmax');

p21min=minlimit21.*p21;%min power loss on q21
p21max=maxlimit21.*p21;%max power loss on q21
subplot(2,2,4)
```

```
plot(x,p21,'--');
hold on
plot(x,p21min);
hold on
plot(x,p21max);
xlabel('Time(s)');
ylabel('Power(W)');
title('Power input with springs on q21');
legend('Optimum Power','Pmin','Pmax');

p22min=minlimit12.*p22;%min power loss on q22
p22max=maxlimit12.*p22;%max power loss on q22
subplot(2,2,2)
plot(x,p22,'--');
hold on
plot(x,p22min);
hold on
plot(x,p22max);
xlabel('Time(s)','FontSize',12);
ylabel('Power(W)','FontSize',12);
title('Power input with springs on q22');
legend('Optimum Power','Pmin','Pmax');
%% Losses Plot
% Plots for the various losses in the system
figure;
subplot(2,2,3)
plot(x,p11); %power on q11
hold on
plot(x,p11+abs(Ploss11)); %power on q11+loss
hold on
plot(x,abs(Ploss11),'black'); %loss on q11
xlabel('Time(s)','FontSize',15);
ylabel('Power(W)','FontSize',15);
title('Power input on q11');
legend('P11','P11+P11loss','P11loss','FontSize',12);

subplot(2,2,1)
plot(x,p12);%power on q12
hold on
plot(x,p12+abs(Ploss12));%power on q12+loss
hold on
plot(x,abs(Ploss12),'black');%loss on q12
xlabel('Time(s)','FontSize',15);
ylabel('Power(W)','FontSize',15);
title('Power input on q12');
legend('P12','P12+P12loss','P12loss','FontSize',12);

subplot(2,2,2)
plot(x,p22);%power on q22
hold on
plot(x,p22+abs(Ploss22));%power on q22+loss
```

```
hold on
plot(x,abs(Ploss22),'black');%loss on q22
xlabel('Time(s)','FontSize',15);
ylabel('Power(W)','FontSize',15);
title('Power input on q22');
legend('P22','P22+P22loss','P22loss','FontSize',12);

subplot(2,2,4)
plot(x,p21);%power on q21
hold on
plot(x,p21+abs(Ploss21));%power on q21+loss
hold on
plot(x,abs(Ploss21),'black');%loss on q21
xlabel('Time(s)','FontSize',15);
ylabel('Power(W)','FontSize',15);
title('Power input on q21');
legend('P21','P21+P21loss','P21loss','FontSize',12);

%% With Springs
%Compensation of losses using springs
figure;
%Losses for q11
subplot(2,2,3)
plot(x,p11min);%min power using spring
hold on
plot(x,p11+abs(Ploss11)); %power on q11+loss
hold on
plot(x,p11max,'black');%max power using spring
xlabel('Time(s)','FontSize',15);
ylabel('Power(W)','FontSize',15);
title('Power input on q11');
legend('Min spring power','P11+P11loss','Max spring power','FontSize',10);

%Losses for q12
subplot(2,2,1)
plot(x,p12min);%min power using spring
hold on
plot(x,p12+abs(Ploss12));%power on q12+loss
hold on
plot (x,p12max,'black');%max power using spring
xlabel('Time(s)','FontSize',15);
ylabel('Power(W)','FontSize',15);
title('Power input on q12');
legend('Min spring power','P12+P12loss','Max spring power','FontSize',10);

%Losses for q22
subplot(2,2,2)
plot(x,p22min);%min power using spring
hold on
```

```
plot(x,p22+abs(Ploss22));%power on q22+loss
hold on
plot(x,p22max,'black');%max power using spring
xlabel('Time(s)','FontSize',15);
ylabel('Power(W)','FontSize',15);
title('Power input on q22');
legend('Min spring power','P22+P22loss','Max spring power','
    FontSize',10);

%Losses for q21
subplot(2,2,4)
plot(x,p21min);%min power using spring
hold on
plot(x,p21+abs(Ploss21));%power on q21+loss
hold on
plot(x,p21max,'black');%max power using spring
xlabel('Time(s)','FontSize',15);
ylabel('Power(W)','FontSize',15);
title('Power input on q21');
legend('Min spring power','P21+P21loss','Max spring power','
    FontSize',10);

%% Efficiency
%calculating the efficiency of the power input on the various DOFs
eta11=[];
eta12=[];
eta21=[];
eta22=[];
for i=1:6284
eta11(i)=abs(p11(i))/(abs(p11(i))+abs(Ploss11(i))); %efficiency on
    q11
eta12(i)=abs(p12(i))/(abs(p12(i))+abs(Ploss12(i))); %efficiency on
    q12
eta21(i)=abs(p21(i))/(abs(p21(i))+abs(Ploss21(i))); %efficiency on
    q21
eta22(i)=abs(p22(i))/(abs(p22(i))+abs(Ploss22(i))); %efficiency on
    q22
end

%plot of the power efficiency of the various DOFs
figure;
subplot(2,2,3)
plot(x,eta11*100)%plot of efficiency of q11
xlabel('Time(s)')
ylabel('Efficiency (\eta) (%)');
title('Efficiency of power input on q11');
subplot(2,2,1)
plot(x,eta12*100)%plot of efficiency of q12
xlabel('Time(s)')
ylabel('Efficiency (\eta) (%)');
title('Efficiency of power input on q12');
```

```
subplot(2,2,4)
plot(x,eta21*100)%plot of efficiency of q21
xlabel('Time(s)')
ylabel('Efficiency (\eta) (%)');
title('Efficiency of power input on q21');
subplot(2,2,2)
plot(x,eta22*100)%plot of efficiency of q22
xlabel('Time(s)')
ylabel('Efficiency (\eta) (%)');
title('Efficiency of power input on q22');

%% Assumption Power Loss and Efficiency Calculation

theta=-180:(360/6283):180; %factor of loss
c=0.14;
% P11loss=c.*Fnetq11.*q11dot.*cos(x).*sign(q11dot);%estimated power loss in q11
% P12loss=c.*Fnetq12.*q12dot.*cos(x).*sign(q12dot);%estimated power loss in q12
% P21loss=c.*Fnetq21.*q21dot.*cos(x).*sign(q21dot);%estimated power loss in q21
% P22loss=c.*Fnetq22.*q22dot.*cos(x).*sign(q22dot);%estimated power loss in q22

P11loss=c.*Fnetq11.*q11dot.*cosd(theta).*sign(q11dot);%estimated power loss in q11
P12loss=c.*Fnetq12.*q12dot.*cosd(theta).*sign(q12dot);%estimated power loss in q12
P21loss=c.*Fnetq21.*q21dot.*cosd(theta).*sign(q21dot);%estimated power loss in q21
P22loss=c.*Fnetq22.*q22dot.*cosd(theta).*sign(q22dot);%estimated power loss in q22

% plot of the estimated power losses
figure;
subplot(2,2,3)
plot(x,p11);%power on q11
hold on
plot(x,p11+abs(P11loss));%power on q11+estimated loss
hold on
plot(x,abs(P11loss),'black');%estimated power loss on q11
xlabel('Time(s)','FontSize',15);
ylabel('Power(W)','FontSize',15);
title('Estimated power loss vs power input on q11');
legend('P11','P11+P11loss','P11loss','FontSize',12);

subplot(2,2,1)
plot(x,p12);%power on q12
hold on
plot(x,p12+abs(P12loss));%power on q12+estimated loss
hold on
```

```
plot(x,abs(P12loss),'black');%estimated power loss on q12
xlabel('Time(s)','FontSize',15);
ylabel('Power(W)','FontSize',15);
title('Estimated Power loss vs power input on q12');
legend('P12','P12+P12loss','P12loss','FontSize',12);
ylim([-0.1 0.15])
subplot(2,2,2)
plot(x,p22);%power on q22
hold on
plot(x,p22+abs(P22loss));%power on q22+estimated loss
hold on
plot(x,abs(P22loss),'black');%estimated power loss on q22
xlabel('Time(s)','FontSize',15);
ylabel('Power(W)','FontSize',15);
title('Estimated power loss vs power input on q22');
legend('P22','P22+P22loss','P22loss','FontSize',12);
ylim([-0.1 0.15])
subplot(2,2,4)
plot(x,p21);%power on q21
hold on
plot(x,p21+abs(P21loss));%power on q21+estimated loss
hold on
plot(x,abs(P21loss),'black');%estimated power loss on q21
xlabel('Time(s)','FontSize',15);
ylabel('Power(W)','FontSize',15);
title('Estimated power loss vs power input on q21');
legend('P21','P21+P21loss','P21loss','FontSize',12);

Rx11=(Fnetq11-c.*Fnetq11)./Fnetq11; % Ratio factor for q11 and q21
Rx12=(Fnetq12-c.*Fnetq12)./Fnetq12; % Ratio factor for q12 and q22

A11=min(Rx11); % Min Ratio factor for q11 and q21
B11=max(Rx11); % Max Ratio factor for q11 and q21
A12=min(Rx12); % Min Ratio factor for q12 and q22
B12=max(Rx12); % Max Ratio factor for q12 and q22

figure;
plot(x,B11*Fnetq11); %Max spring force limit for q11 and q21
hold on;
plot(x,Fnetq11,'--'); %Spring force optimum estimated
hold on;
plot(x,A11*Fnetq11,'black'); %Minimum spring force limit for q11 and q21
xlabel('Time(s)','FontSize',15);
ylabel('Force(N)','FontSize',15);
legend('Fqmax','Fspring11/21','Fqmin','FontSize',12);
title('Estimated Compensation force for bottom pulleys q11 and q21');

figure;
plot(x,B12*Fnetq12);%Maximum spring force limit for q12 and q22
```

```
hold on;
plot(x,Fnetq12,'--'); %Spring force optimum estimated
hold on;
plot(x,A12*Fnetq12,'black');%Minimum spring force limit for q12 and q22
xlabel('Time(s)','FontSize',15);
ylabel('Force(N)','FontSize',15);
legend('Fqmax','Fspring12/22','Fqmin','FontSize',12);
title('Estimated Compensation force for bottom pulleys q12 and q22');
%% Estimated Efficiency
e11=[];
e12=[];
e21=[];
e22=[];
for i=1:6284
e11(i)=abs(p11(i))/(abs(p11(i))+abs(P11loss(i))); %Estimated power efficiency for q11
e12(i)=abs(p12(i))/(abs(p12(i))+abs(P12loss(i))); %Estimated power efficiency for q12
e21(i)=abs(p21(i))/(abs(p21(i))+abs(P21loss(i))); %Estimated power efficiency for q21
e22(i)=abs(p22(i))/(abs(p22(i))+abs(P22loss(i))); %Estimated power efficiency for q22
end
%Plots of the estimated efficiencies of power input on the various DOFs
figure;
subplot(2,2,3)
plot(x,e11*100)%plot of estimated efficiency on q11
xlabel('Time(s)')
ylabel('Efficiency (\eta) (%)');
title('Estimated Efficiency of power input on q11');
subplot(2,2,1)
plot(x,e12*100)%plot of estimated efficiency on q12
xlabel('Time(s)')
ylabel('Efficiency (\eta) (%)');
title('Estimated Efficiency of power input on q12');
subplot(2,2,4)
plot(x,e21*100)%plot of estimated efficiency on q21
xlabel('Time(s)')
ylabel('Efficiency (\eta) (%)');
title('Estimated Efficiency of power input on q21');
subplot(2,2,2)
plot(x,e22*100)%plot of estimated efficiency on q22
xlabel('Time(s)')
ylabel('Efficiency (\eta) (%)');
title('Estimated Efficiency of power input on q22');
%% Compensation Springs
%Compensation of losses using springs
figure;
```

```
Pcomp11=Fcomp21.*q11dot;
Pcomp12=Fcomp12.*q12dot;
Pcomp21=Fcomp21.*q21dot;
Pcomp22=Fcomp12.*q22dot;

% Pcomp11=(Fnetq11./140-0.01).*q11dot;
% Pcomp12=(Fnetq12./140-0.01).*q12dot;
% Pcomp21=(Fnetq21./140-0.01).*q21dot;
% Pcomp22=(Fnetq22./140-0.01).*q22dot;
%Losses for q11
subplot(2,2,3)
plot(x,p11+abs(Pcomp11),'LineWidth',1);%power with compensation springs
hold on
plot(x,p11+abs(Ploss11),'--','LineWidth',2); %power on q11+loss
hold on
plot(x,abs(Ploss11-Pcomp11),'black');%power loss
xlabel('Time(s)','FontSize',15);
ylabel('Power(W)','FontSize',15);
title('Power input on q11');
legend('P11+P11comp','P11+P11loss','P11loss','FontSize',12);

%Losses for q12
subplot(2,2,1)
plot(x,p12+abs(Pcomp12),'LineWidth',1);%power with compensation springs
hold on
plot(x,p12+abs(Ploss12),'--','LineWidth',2);%power on q12+loss
hold on
plot (x,abs(Ploss12-Pcomp12),'black');%power loss
xlabel('Time(s)','FontSize',15);
ylabel('Power(W)','FontSize',15);
title('Power input on q12');
legend('P12+P12comp','P12+P12loss','P12loss','FontSize',12);

%Losses for q22
subplot(2,2,2)
plot(x,p22+abs(Pcomp22),'LineWidth',1);%power with compensation springs
hold on
plot(x,p22+abs(Ploss22),'--','LineWidth',2);%power on q22+loss
hold on
plot(x,abs(Ploss22-Pcomp22),'black');%power loss
xlabel('Time(s)','FontSize',15);
ylabel('Power(W)','FontSize',15);
title('Power input on q22');
legend('P22+P22comp','P22+P22loss','P22loss','FontSize',12);

%Losses for q21
subplot(2,2,4)
```

```
plot(x,p21+abs(Pcomp21),'LineWidth',1);%power with compensation springs
hold on
plot(x,p21+abs(Ploss21),'--','LineWidth',2);%power on q21+loss
hold on
plot(x,abs(Ploss21-Pcomp21),'black');%power loss
xlabel('Time(s)','FontSize',15);
ylabel('Power(W)','FontSize',15);
title('Power input on q21');
legend('P21+P21comp','P21+P21loss','P21loss','FontSize',12);
%% Efficiency using compensation springs
ecomp11=[];
ecomp12=[];
ecomp21=[];
ecomp22=[];
for i=1:6284
ecomp11(i)=(abs(p11(i))+abs(Pcomp11(i)))/(abs(p11(i))+abs(Ploss11(i))); %Estimated power efficiency for q11
ecomp12(i)=(abs(p12(i))+abs(Pcomp12(i)))/(abs(p12(i))+abs(Ploss12(i))); %Estimated power efficiency for q12
ecomp21(i)=(abs(p21(i))+abs(Pcomp21(i)))/(abs(p21(i))+abs(Ploss21(i))); %Estimated power efficiency for q21
ecomp22(i)=(abs(p22(i))+abs(Pcomp22(i)))/(abs(p22(i))+abs(Ploss22(i))); %Estimated power efficiency for q22
end
%Plots of the estimated efficiencies of power input on the various DOFs
figure;
subplot(2,2,3)
plot(x,ecomp11,'LineWidth',1.5)%plot of efficiency on q11 using springs
xlabel('Time(s)','FontSize',12)
ylabel('Efficiency (\eta)','FontSize',12);
title('q11');
subplot(2,2,1)
plot(x,ecomp12,'LineWidth',1.5)%plot of efficiency on q12 using springs
xlabel('Time(s)','FontSize',12)
ylabel('Efficiency (\eta)','FontSize',12);
title('q12');
subplot(2,2,4)
plot(x,ecomp21,'LineWidth',1.5)%plot of efficiency on q21 using springs
xlabel('Time(s)','FontSize',12)
ylabel('Efficiency (\eta)','FontSize',12);
title('q21');
subplot(2,2,2)
plot(x,ecomp22,'LineWidth',1.5)%plot of efficiency on q22 using springs
xlabel('Time(s)','FontSize',12)
ylabel('Efficiency (\eta)','FontSize',12);
```

```
title('q22');
```

Bibliography

(2020)), *Friction Coefficients.* https://www.tribology-abc.com/abc/polymers.htm

Albu-Schäffer, A., S. Wolf, O. Eiberger, S. Haddadin, F. Petit and M. Chalon (2010), Dynamic modelling and control of variable stiffness actuators, in *2010 IEEE International Conference on Robotics and Automation*, IEEE, pp. 2155–2162.

Barents, R., M. Schenk, W. D. van Dorsser, B. M. Wisse and J. L. Herder (2011), Spring-to-spring balancing as energy-free adjustment method in gravity equilibrators, **vol. 133**, no.6, p. 061010.

Groothuis, S. S., R. Carloni and S. Stramigioli (2016), Single motor-variable stiffness actuator using bistable switching mechanisms for independent motion and stiffness control, in *2016 IEEE International Conference on Advanced Intelligent Mechatronics (AIM)*, IEEE, pp. 234–239.

Groothuis, S. S., N. Manourat and S. Stramigioli (2020), Novel Cable-driven Variable Impedance Mechanism, *Submitted to Robotics and Automation Letters / International Conference on Robotics and Automation.*

Groothuis, S. S., G. Rusticelli, A. Zucchelli, S. Stramigioli and R. Carloni (2012), The vsaUT-II: A novel rotational variable stiffness actuator, in *2012 IEEE International Conference on Robotics and Automation*, IEEE, pp. 3355–3360.

Groothuis, S. S., G. Rusticelli, A. Zucchelli, S. Stramigioli and R. Carloni (2013), The variable stiffness actuator vsaUT-II: Mechanical design, modeling, and identification, **vol. 19**, no.2, pp. 589–597.

Ham, R. v., T. Sugar, B. Vanderborght, K. Hollander and D. Lefeber (2009), Compliant actuator designs, **vol. 3**, no.16, pp. 81–94.

Herder, J. L. (2001), *Energy-free Systems. Theory, conception and design of statically*, volume 2.

Herder, J. L., R. Barents, B. M. Wisse and W. D. Van Dorsser (2011), Efficiently variable zero stiffness mechanisms, in *4th International Workshop on Human-Friendly Robotics, The Netherlands.*

Jafari, A. (2014), Coupling between the output force and stiffness in different variable stiffness actuators, in *Actuators*, volume 3, Multidisciplinary Digital Publishing Institute, pp. 270–284.

Jafari, A., N. G. Tsagarakis and D. G. Caldwell (2011), AwAS-II: A new actuator with adjustable stiffness based on the novel principle of adaptable pivot point and variable lever ratio, in *2011 IEEE International Conference on Robotics and Automation*, IEEE, pp. 4638–4643.

Jafari, A., H. Q. Vu and F. Iida (2016), Determinants for stiffness adjustment mechanisms, **vol. 82**, no.3-4, pp. 435–454.

Laffranchi, M., N. G. Tsagarakis, F. Cannella and D. G. Caldwell (2009), Antagonistic and series elastic actuators: a comparative analysis on the energy consumption, in *2009 IEEE/RSJ International Conference on Intelligent Robots and Systems*, IEEE, pp. 5678–5684.

Liu, Y., X. Liu, Z. Yuan and J. Liu (2019), Design and analysis of spring parallel variable stiffness actuator based on antagonistic principle, *Mechanism and Machine Theory*, **vol. 140**, pp. 44–58.

Loughlin, C., A. Albu-Schäffer, S. Haddadin, C. Ott, A. Stemmer, T. Wimböck and G. Hirzinger (2007), The DLR lightweight robot: design and control concepts for robots in human environments, *Industrial Robot: an international journal.*

Manourat, N. (2019), The Development of a Cable-driven Variable Stiffness Mechanism Test Bed.

Petit, F. and A. Albu-Schäffer (2011), State feedback damping control for a multi dof variable stiffness robot arm, in *2011 IEEE international conference on robotics and automation*, IEEE, pp. 5561–5567.

Petit, F., M. Chalon, W. Friedl, M. Grebenstein, A. Albu-Schäffer and G. Hirzinger (2010), Bidirectional antagonistic variable stiffness actuation: Analysis, design & implementation, in *2010 IEEE International Conference on Robotics and Automation*, IEEE, pp. 4189–4196.

Pratt, G. A. and M. M. Williamson (1995), Series elastic actuators, in *Proceedings 1995 IEEE/RSJ International Conference on Intelligent Robots and Systems. Human Robot Interaction and Cooperative Robots*, volume 1, IEEE, pp. 399–406.

Spagnuolo, G., M. Malosio, T. Dinon, L. M. Tosatti and G. Legnani (2017), Analysis and synthesis of LinWWC-VSA, a Variable Stiffness Actuator for linear motion, *Mechanism and Machine Theory*, **vol. 110**, pp. 85–99.

Sun, J., Z. Guo, D. Sun, S. He and X. Xiao (2018), Design, modeling and control of a novel compact, energy-efficient, and rotational serial variable stiffness actuator (SVSA-II), *Mechanism and Machine Theory*, **vol. 130**, pp. 123–136.

Van Geffen, V. (2009), A study of friction models and friction compensation.

Vanderborght, B., A. Albu-Schäffer, A. Bicchi, E. Burdet, D. G. Caldwell, R. Carloni, M. Catalano, O. Eiberger, W. Friedl, G. Ganesh et al. (2013), Variable impedance actuators: A review, **vol. 61**, no.12, pp. 1601–1614.

Visser, L. C., R. Carloni and S. Stramigioli (2011), Energy-efficient variable stiffness actuators, **vol. 27**, no.5, pp. 865–875.

Wolf, S., G. Grioli, O. Eiberger, W. Friedl, M. Grebenstein, H. Höppner, E. Burdet, D. G. Caldwell, R. Carloni, M. G. Catalano et al. (2015), Variable stiffness actuators: Review on design and components, **vol. 21**, no.5, pp. 2418–2430.